



# A Quick Look at the 3 GHz Radio Sky. I. Source Statistics from the Very Large Array Sky Survey

Yjan A. Gordon<sup>1</sup> , Michelle M. Boyce<sup>1</sup> , Christopher P. O'Dea<sup>1</sup> , Lawrence Rudnick<sup>2</sup> , Heinz Andernach<sup>3</sup> , Adrian N. Vantyghem<sup>1</sup> , Stefi A. Baum<sup>1</sup>, Jean-Paul Bui<sup>4</sup>, Mathew Dionyssiou<sup>4</sup>, Samar Safi-Harb<sup>1</sup> , and Isabel Sander<sup>1</sup>

<sup>1</sup> Department of Physics and Astronomy, University of Manitoba, Winnipeg, MB R3T 2N2, Canada; [yjan.gordon@umanitoba.ca](mailto:yjan.gordon@umanitoba.ca)

<sup>2</sup> Minnesota Institute for Astrophysics, School of Physics and Astronomy, University of Minnesota, 116 Church Street SE, Minneapolis, MN 55455, USA

<sup>3</sup> Departamento de Astronomía, DCNE, Universidad de Guanajuato, Cjón de Jalisco s/n, 36023 Guanajuato, GTO, Mexico

<sup>4</sup> Dunlap Institute for Astronomy and Astrophysics, University of Toronto, 50 St George Street, Toronto, ON M5S 3H4, Canada

Received 2021 February 22; revised 2021 May 18; accepted 2021 May 25; published 2021 August 13

## Abstract

The Very Large Array Sky Survey (VLASS) is observing the entire sky north of  $-40^\circ$  in the  $S$  band ( $2 \text{ GHz} < \nu < 4 \text{ GHz}$ ), with the highest angular resolution ( $2.\overset{\prime}{5}$ ) of any all-sky radio continuum survey to date. VLASS will cover its entire footprint over three distinct epochs, the first of which has now been observed in full. Based on *Quick Look* images from this first epoch, we have created a catalog of  $1.9 \times 10^6$  reliably detected radio components. Due to the limitations of the *Quick Look* images, component flux densities are underestimated by  $\sim 15\%$  at  $S_{\text{peak}} > 3 \text{ mJy beam}^{-1}$  and are often unreliable for fainter components. We use this catalog to perform statistical analyses of the  $\nu \sim 3 \text{ GHz}$  radio sky. Comparisons with the Faint Images of the Radio Sky at Twenty-Centimeters (FIRST) survey show the typical  $1.4\text{--}3 \text{ GHz}$  spectral index,  $\alpha$ , to be  $\sim -0.71$ . The radio color–color distribution of point and extended components is explored by matching with FIRST and the LOFAR Two-meter Sky Survey. We present the VLASS source counts,  $dN/dS$ , which are found to be consistent with previous observations at  $1.4$  and  $3 \text{ GHz}$ . Resolution improvements over FIRST result in excess power in the VLASS two-point correlation function at angular scales  $\lesssim 7''$ , and in  $18\%$  of active galactic nuclei associated with a single FIRST component being split into multicomponent sources by VLASS.

Unified Astronomy Thesaurus concepts: [Radio astronomy \(1338\)](#); [Radio galaxies \(1343\)](#); [Radio source catalogs \(1356\)](#); [Sky surveys \(1464\)](#)

## 1. Introduction

The past two decades have seen the advent of wide-field continuum imaging surveys of the radio sky. The advantages of blind surveys over targeted observations include large numbers of objects for which observations are obtained and the potential to discover new phenomena (Padovani 2016; Norris 2017). The National Radio Astronomy Observatory (NRAO) Very Large Array Sky Survey (NVSS; Condon et al. 1998) set the bar for wide-field radio continuum surveys by surveying 80% of the sky at  $1.4 \text{ GHz}$ . With an angular resolution of  $\sim 45''$  and a typical rms noise of  $450 \mu\text{Jy beam}^{-1}$ , NVSS has cataloged  $\sim 2 \times 10^6$  radio detections. The Faint Images of the Radio Sky at Twenty-Centimeters (FIRST; Becker et al. 1995) survey, also at  $1.4 \text{ GHz}$ , probes deeper than NVSS with an rms of  $130 \mu\text{Jy beam}^{-1}$  and improved angular resolution of  $5.\overset{\prime}{4}$  while covering 25% of the sky. Meanwhile, at low frequency the Tata Institute of Fundamental Research Giant Metre Radio Telescope Sky Survey (TGSS; Intema et al. 2017) has mapped 90% of the sky at  $150 \text{ MHz}$  with an rms of  $5 \text{ mJy beam}^{-1}$  and an angular resolution of  $\sim 25''$ .

Technological improvements over the past two decades have allowed upgrades to existing radio telescopes such as the Karl G. Jansky Very Large Array (VLA) and the construction of new facilities such as the Low Frequency Array (LOFAR; van Haarlem et al. 2013), the Australian Square Kilometre Array Pathfinder (ASKAP; Johnston et al. 2007), and the MeerKAT telescope (Jonas 2009). These state-of-the-art facilities allow for sky surveys that probe deeper, with shorter observing times, and with higher resolution than were previously possible, allowing us to build on the scientific output of the last

generation of continuum sky surveys. For instance, ASKAP is being used to conduct the Rapid ASKAP Continuum Survey (RACS; McConnell et al. 2020) and Evolutionary Map of the Universe (EMU; Norris et al. 2011) survey, providing  $\nu \sim 1 \text{ GHz}$  coverage of the southern sky, the latter down to sensitivities of  $\sim 10 \mu\text{Jy beam}^{-1}$ . Meanwhile, the LOFAR Two-meter Sky Survey (LoTSS; Shimwell et al. 2017) will survey the entire northern sky at  $\sim 150 \text{ MHz}$  with a synthesized beam size of  $6''$  and an rms of  $\sim 70 \mu\text{Jy beam}^{-1}$ , providing deep, low-frequency observations to complement existing high-frequency data.

Of the current generation of radio continuum imaging surveys, the highest angular resolution will be provided by the VLA Sky Survey (VLASS; Lacy et al. 2020). With an angular resolution of  $\sim 2.\overset{\prime}{5}$ , VLASS is currently surveying the entire sky north of  $-40^\circ$  in the  $S$  band ( $2 \text{ GHz} < \nu < 4 \text{ GHz}$ , hereafter referred to as  $\nu \sim 3 \text{ GHz}$ ). Such a small beam size has the advantage of revealing morphological structure on smaller angular scales than other surveys—e.g., many sources that appear compact in FIRST or LoTSS may be resolved by VLASS. Furthermore, the resolution of VLASS allows improved study of the true sizes of radio sources in the sky (e.g., Allen et al. 1962; Cotton et al. 2018), as well as more reliable identifications of their optical or infrared hosts. Survey operations for VLASS began in 2017, and observing for the first of three planned epochs was completed in 2019.

In this paper we describe a catalog of radio components produced from the VLASS epoch 1 *Quick Look* imaging. Here and throughout we use the term *radio component* to refer to a single detection by the source-finding algorithm rather than *radio source*, as, especially at high resolution, a single physical

radio *source* may be described by multiple components. For example, the two hot spots of a double-lobed radio galaxy may appear as two different *components* in the catalog while still belonging to the same physical *source*. Host galaxy identifications for detections in this catalog will be detailed in an upcoming work (Y. A. Gordon et al., 2021 in preparation).

The data used and the production of the VLASS epoch 1 *Quick Look* component catalog are described in Section 2. The rapid CLEANing of the *Quick Look* images leads to limitations of the scientific usefulness of this catalog, and these are described in Section 3. We match our catalog to  $\nu \sim 1.4$  GHz and  $\nu \sim 150$  MHz data from FIRST and LoTSS, respectively, in Section 4, and present the resultant spectral index and spectral curvature distributions. In Section 5 we present the VLASS source counts. We use our catalog to explore the size distribution of VLASS components in Section 6. This is complemented by an analysis of the VLASS two-point correlation function and by exploring the impact of a factor of  $\sim 2$  improvement in angular resolution over FIRST. A summary of this paper is given in Section 7. Throughout this work we adopt the convention  $S_\nu \propto \nu^\alpha$  for radio spectral index measurements and assume a flat  $\Lambda$ CDM cosmology with  $h = 0.7$ ,  $H_0 = 100h \text{ km s}^{-1} \text{ Mpc}^{-1}$ ,  $\Omega_M = 0.3$ , and  $\Omega_\Lambda = 0.7$ .

## 2. Catalog Production

### 2.1. VLASS Quick Look Images

The first-epoch observations from VLASS are currently available as rapidly processed *Quick Look* images. In this paper we describe a catalog of radio components produced using these images, the availability of which was first announced in Gordon et al. (2020). These *Quick Look* images are produced by NRAO and made available within weeks of the observations being conducted. However, the expedited nature of the image processing limits their quality and hence constrains their scientific usability. Furthermore, this rapid-CLEAN process employed by NRAO was updated between epochs 1.1 and 1.2, resulting in significant differences in image quality between the two subepochs.<sup>5</sup> The epoch 1 *Quick Look* images are described in full in Lacy et al. (2019), but we highlight here the key issues known in advance:

1. Flux calibration—The flux density values in the *Quick Look* images are on average systematically low by  $\sim 10\%$ . Furthermore, Lacy et al. (2019) show that there is a substantial scatter,  $\sim 15\%$ , in the ratio of flux densities measured by VLASS and pointed observations of calibrator targets.
2. Astrometry—The positional accuracy of the VLASS *Quick Look* imaging is limited to  $\sim 1''$ . This improves to  $0''.5$  at decl., decl.,  $> -20^\circ$ .
3. Ghosts—These appear offset by multiples of  $\sim 3'$  in right ascension, R.A., east of bright sources. The *Quick Look* image production pipeline is designed to flag and remove these, but some faint ghosts may still remain. Moreover, the removal of ghosts was refined between epochs 1.1 and 1.2, meaning that the earlier images are more likely to contain residual faint ghosts.

The impact of these reliability issues on our component catalog is further detailed in Section 3.

<sup>5</sup> 49.9% and 50.1% of the imaging was performed in epochs 1.1 and 1.2, respectively.

The full epoch 1 *Quick Look* image set consists of 35,285 1 deg<sup>2</sup> *Quick Look* images (hereafter referred to as subtiles) across 899  $\sim 40$  deg<sup>2</sup> VLASS observing tiles (Kimball 2017). The catalog based on these data and used in this paper has been made available to the community via <https://cirada.ca/catalogs> (Gordon et al. 2020), and its production is described below. An extensive User Guide is also available for download with the catalog, and we recommend reading this prior to accessing the data.

### 2.2. Component Extraction and Duplicate Finding

For each of the 35,285 subtiles in VLASS, the source extraction code Python Blob Detection and Source Finding (PyBDSF; Mohan & Rafferty 2015) was run in “srl” mode—meaning that a list of components is provided rather than a list of individual Gaussian fits. The method adopted by PyBDSF is to detect flux islands at  $3\sigma$  above the image mean (where  $\sigma$  is the local rms) and then fit components composed of one or more Gaussians within those islands with a peak brightness at  $5\sigma$  above the image mean. For the most part the default PyBDSF parameters are used, with two exceptions:

1. The sliding box used by PyBDSF to calculate the rms is set at a fixed size of  $200 \times 200$  pixels with a slide step of 50 pixels. Explicitly, the argument `rms_box = {200, 50}` is called when running PyBDSF. The pixels in the subtiles are 1'' square.
2. For completeness PyBDSF is set to output detected islands of flux density to which it did not fit components in addition to the list of fitted components it finds. This is achieved by running PyBDSF with the argument `inc_empty = True`, and such detections are included and identified in the catalog by `S_Code == "E."` These “empty islands” are generally faint, with 95% of such detections having a peak brightness of less than 2 mJy beam<sup>-1</sup>.

The resultant 35,285 individual PyBDSF component tables for each subtitle are then merged into a single table. As there is a  $\sim 2'$  overlap region between the images, the catalog contains duplicate entries that refer to the same component. Based on the beam size and the positional uncertainty associated with the images, we use a 2'' search radius around each component to identify duplicates. Where component duplicates are identified, preference is given to the component with the highest ratio of peak brightness to local rms. All duplicates are retained within the catalog but are flagged as such (0 = unique component; 1 = duplicate component that is the preferred version of this component; 2 = duplicate component that is not the preferred version of this component). To select a duplicate-free list of components, only components with `Duplicate_flag < 2` are used for the statistics presented in this work.

### 2.3. Reliability of Detections

In addition to the basic measurements provided by PyBDSF, we wish to determine which detected components are real, as opposed to false-positive detections. A column, `Quality_flag`, is provided in our catalog to highlight our recommended components to use based on analysis of the raw output. This takes account of three different parameters that are combined into a single integer flag value:

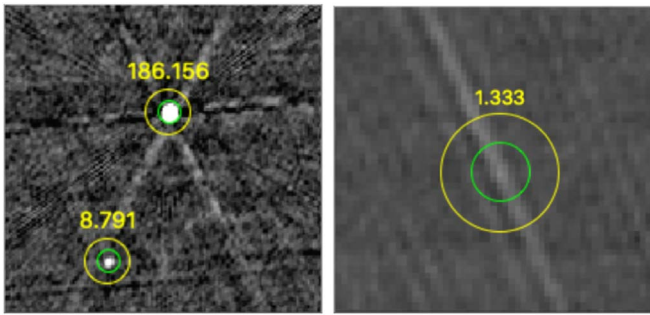


**Figure 1.** The “peak-to-ring” metric is specifically designed to catch false-positive components that have been fit to artifacts, and more specifically sidelobes. In these images the green ring shows the inner radius ( $5''$ ) and the yellow ring the outer radius ( $10''$ ) of the annulus in which flux density is compared to the component peak brightness. The left panel shows two good component detections with high peak-to-ring values. The right panel shows a component erroneously fitted to a sidelobe. In this case the ratio of peak brightness to maximum flux in the annulus is only 1.33, demonstrating that lower peak-to-ring values have diagnostic value in flagging false detections.

1. The ratio of the total flux density and peak brightness measurements. Given the reliability issues associated with the *Quick Look* images, any component where the total flux is less than the peak brightness should be considered to be a possibly dubious measurement. Thus, we flag components with  $S_{\text{peak}} > S_{\text{total}}$  by setting  $\text{Quality\_flag} = \text{Quality\_flag} + 4$ .
2. The signal-to-noise ratio (S/N) of the component. We flag components with a peak brightness lower than 5 times the local rms and set  $\text{Quality\_flag} = \text{Quality\_flag} + 2$ . Nearly all components flagged here have  $3 < \text{S/N} < 5$ ; however, we note that 1600 components have  $\text{S/N} < 3$ . This is attributed to differences in the local rms from the rms image used to detect the islands, as well as the fitted island rms.
3. The ratio of peak brightness to the maximum flux density in a ring centered on the component position and with inner and outer radii of  $5''$  and  $10''$ , respectively. This is specifically designed to identify potential sidelobe structures that have erroneously been fitted as components. Sidelobes should have a low value for this ratio compared to true components that are surrounded by just the background noise (see Figure 1). A caveat here is that close double radio sources, the detection of which should be a forte of VLASS, will also provide low values to this ratio and could thus be inadvertently identified as sidelobe detections. In light of this, this metric is only used to flag components that are more than  $20''$  from another component and with  $\text{Peak\_to\_ring} < 2$ . Here we apply  $\text{Quality\_flag} = \text{Quality\_flag} + 1$ .

The combination of these parameters gives a single flag with an integer value between 0 and 7. In Figure 2 we show examples of our quality flagging routine identifying spurious detections due to image artifacts around bright components.

In Figure 3 we compare the peak brightness distributions for all components with components that have  $\text{Quality\_flag} == 0$ . The distribution for components that have not been flagged shows a reduced number of faint detections. Although this demonstrates that suspect detections are generally faint, note that the distribution for unflagged components deviates from the flagged component peak brightness distribution up to  $\sim 5 \text{ mJy beam}^{-1}$ . Therefore, to select only the most reliable measurements, we recommend using

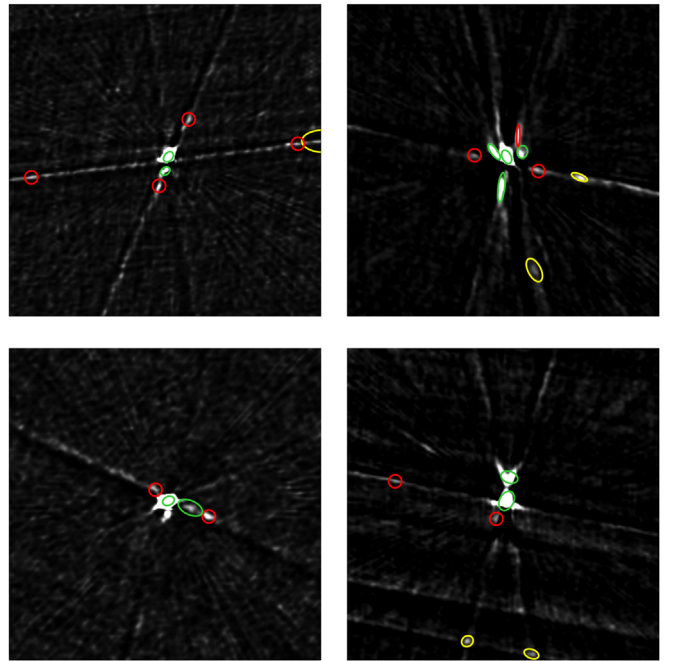


**Figure 2.** Sample cutouts of  $2' \times 2'$ , centered on bright components demonstrating the sidelobes that the *Quick Look* processing pipeline has failed to clean. These artifacts can then be detected by PyBDSF as spurious components. Here green ellipses show components that our algorithm does not flag, yellow ellipses show components that our algorithm does flag, and red circles indicate where PyBDSF has detected a flux island but not fitted a component. The ellipse geometry is defined by the component parameters and enlarged by 50% for clarity.

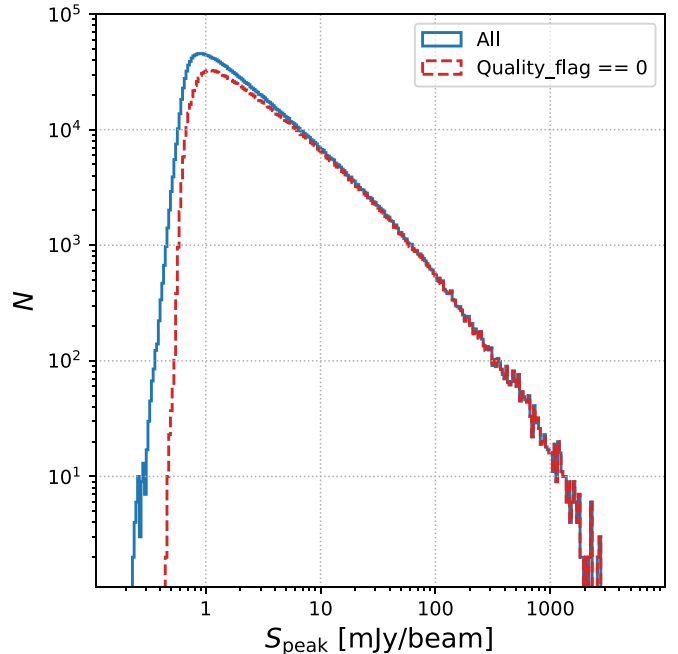


**Figure 3.** The distribution of peak brightness measurements from our catalog. The blue line shows the distribution for all fitted components, including those that do not have  $\text{Quality\_flag} == 0$  (empty flux islands are not included here). The red line shows the flux distribution for only those components with  $\text{Quality\_flag} == 0$ . Note the excess of low flux densities when using all components.

$\text{Quality\_flag} == 0$ , indicating that the component has not been flagged for any of the above quality issues, in addition to just applying simple brightness cuts to the data.

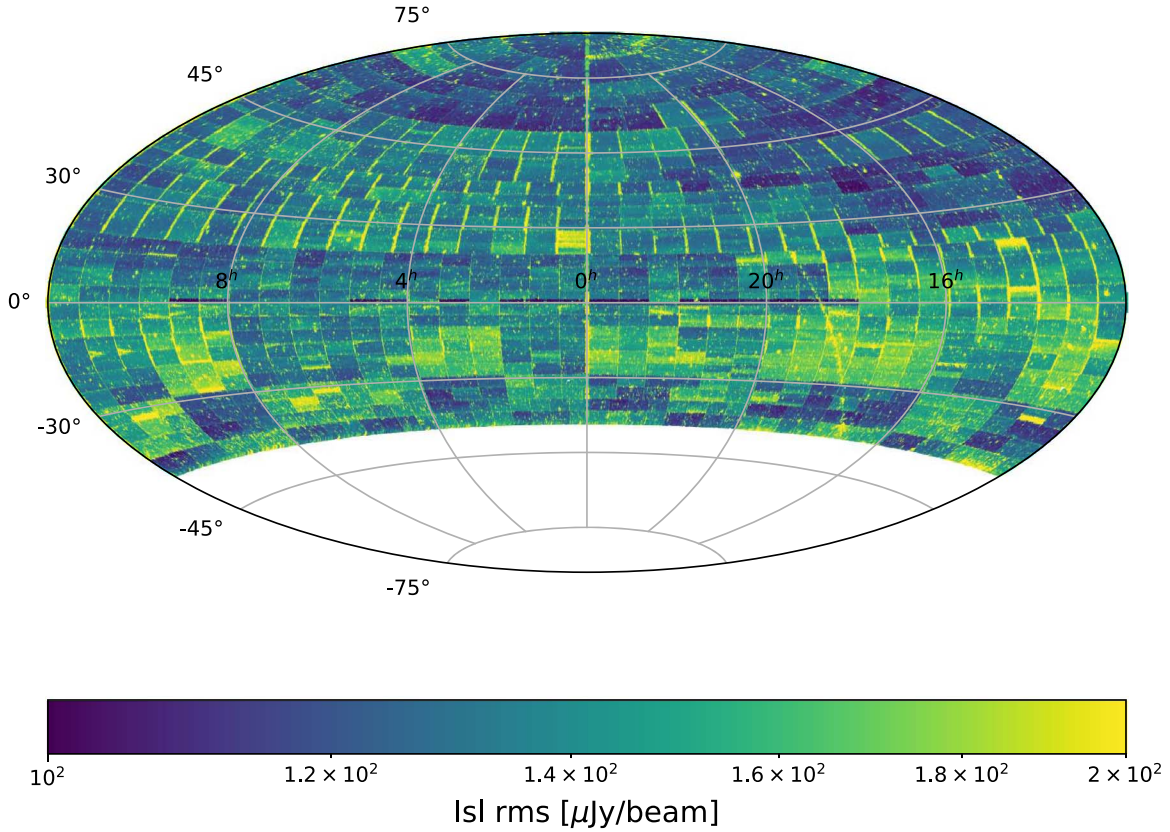


**Figure 4.** Aitoff projection in equatorial (J2000) coordinates of the rms values found around all VLASS components. For clarity only  $100 \mu\text{Jy beam}^{-1} < \text{IsI\_rms} < 200 \mu\text{Jy beam}^{-1}$  are shown and on a  $\log_{10}$  scale. Additionally, this is limited to components with  $\text{Quality\_flag} == 0$  and  $\text{Duplicate\_flag} < 2$ . From this plot it is clear that the depth of the *Quick Look* imaging is not homogeneous. Key features in this plot include the Galactic plane at low Galactic longitudes, the checkerboard pattern at southern latitudes, high noise at the east–west boundaries of tiles, and a region of high noise at decl.  $\sim +85^\circ$  in the western hemisphere ( $12 \text{ hr} < \text{R.A.} < 24 \text{ hr}$ ).

While not explicitly provided by PyBDSF when set to provide component lists, we recover the pixel coordinates of components based on the image header information and provide them as additional information. Further information on the VLASS tile and subtle to which a detection belongs, as well as angular separation from the nearest other component (given in the column *NN\_dist* for components with *Duplicate\_flag*  $< 2$  and *Quality\_flag*  $= 0$ ), is included. Additionally, we provide the angular separations from the nearest detections in the two previous NRAO wide-field continuum surveys, NVSS and FIRST, as the columns *NVSS\_distance* and *FIRST\_distance*,<sup>6</sup> respectively. The latter two metrics may be useful to further assess the reliability of the detection (particularly for fainter sources) and for finding potential variable objects (in which case we urge caution on the part of the user and remind them of the systematic underestimation of fluxes in the VLASS *Quick Look* imaging). The resultant component catalog consists of 3,381,277 rows, where each row corresponds to a detected component or empty flux island. Of these, 1,692,158 have *Duplicate\_flag*  $< 2$  and *Quality\_flag*  $= 0$ .

S\_code !='E' not included

### 3. Data Quality

Here we detail the issues with data both known about from Lacy et al. (2019) and discovered during our quality assurance

testing. While the major known issues are described here, this list is unlikely to be comprehensive.<sup>7</sup>

#### 3.1. Noise Variation between Images

Between epochs 1.1 and 1.2 the VLASS *Quick Look* image pipeline was upgraded to include automatic as opposed to manual flagging of science data. While reducing the human workload, this automatic routine increased the amount of flagging, resulting in a reduced bandwidth and thus noisier data (M. Lacy 2021, private communication). It follows that these differences in the image processing between the two data sets will have an impact on the sample homogeneity. The median rms for images from epoch 1.1 is  $128 \mu\text{Jy beam}^{-1}$ , compared to  $145 \mu\text{Jy beam}^{-1}$  for epoch 1.2, indicating the impact of the change of image processing methods on the data. In Figure 4 we show an Aitoff projection of the local rms around components in our catalog. Inspecting this plot shows several curious features highlighting the lack of homogeneity of the VLASS *Quick Look* imaging. In particular, users of this catalog should be aware of the following:

1. At southern declinations a “checkerboard” pattern of rms is apparent. This clear patterning is indicative of variation between VLASS tiles, and moreover of the difference

<sup>6</sup> As FIRST only covers around 1/3 of the VLASS footprint, *FIRST\_distance* should only be considered useful within the FIRST footprint.

<sup>7</sup> We encourage users to report any additional issues they encounter with these data via the catalog feedback portal at <https://cirada.ca/catalogs>.

- between the two subepochs (see also the VLASS tiling pattern described in Kimball 2017).
2. At northern latitudes in particular, high noise levels are visible at the east–west boundaries of VLASS tiles. The increase in noise at specifically the east–west boundary is likely attributable to the fact that some tile edges were flagged to avoid unreliable fluxes associated with online software bugs related to the ghosts (Lacy et al. 2019).
  3. There is a region of high noise that stands out at decl.  $\sim +85^\circ$  and 12 hr  $< \text{R.A.} < 24$  hr.
  4. The Galactic plane is clearly visible as a region of enhanced noise, albeit only at very low Galactic latitudes ( $|b| \lesssim 0.5^\circ$ ) and for a relatively narrow range of Galactic longitudes ( $350^\circ \lesssim l \lesssim 50^\circ$ ).
  5. There are several strips at  $0^\circ < \text{decl.} < +1^\circ$  that have lower noise ( $\sim 100 \mu\text{Jy beam}^{-1}$ ). This is the result of accidentally observing these regions twice during survey operations and using both observations in the production of the *Quick Look* images. This deeper VLASS region has a total area of  $\sim 160 \text{ deg}^2$ .

### 3.2. Reliability of Flux Density Measurements

From Lacy et al. (2019) we know that the flux densities in the VLASS *Quick Look* imaging are systematically underestimated. Based on comparisons with  $>50$  VLA calibrator sources, Lacy et al. (2019) estimate that the peak brightness in the VLASS *Quick Look* images is underestimated by  $\sim 15\%$ , and the total flux density of components is underestimated by  $\sim 10\%$ . Lacy et al. (2019) report a scatter of about 8% in these measurements. In this section we compare the flux density measurements in our catalog to existing survey data so as to obtain our own estimate of the VLASS flux density reliability.

#### 3.2.1. Direct Comparisons with Other 3 GHz Data

One approach to measure the impact of the potential flux density underestimation of the VLASS *Quick Look* images on our catalog is to directly compare our measurements to existing 3 GHz flux densities for components in our catalog. However, previous blind continuum observations at this frequency have come from deep, narrow-field surveys (Vernstrom et al. 2016; Smolčić et al. 2017), limiting the overlap in detected components with VLASS. Of the available 3 GHz catalogs, the **VLA-COSMOS 3 GHz Large project** (hereafter referred to simply as VLA-COSMOS; Smolčić et al. 2017), covering the  $2 \text{ deg}^2$  of the COSMOS field, presents the largest overlap with VLASS in terms of sensitivity and sky coverage. Our VLASS catalog contains 131 components with a VLA-COSMOS detection within  $2.^{\circ}5$  (126 of these are separated by less than  $1''$ ).

The small number of overlapping components between VLASS and VLA-COSMOS limits our ability to perform a robust flux calibration of our catalog via a direct comparison of the independent flux density measurements at 3 GHz. Nonetheless, we report here our findings in comparing the measurements from both catalogs. Given the already small sample size, for this comparison we do not account for the difference in resolution between VLA-COSMOS ( $0.^{\circ}75$ ) and VLASS. In Figure 5 we show the ratio of VLASS to VLA-COSMOS flux density measurements for the 131 matched components as a function of peak brightness in

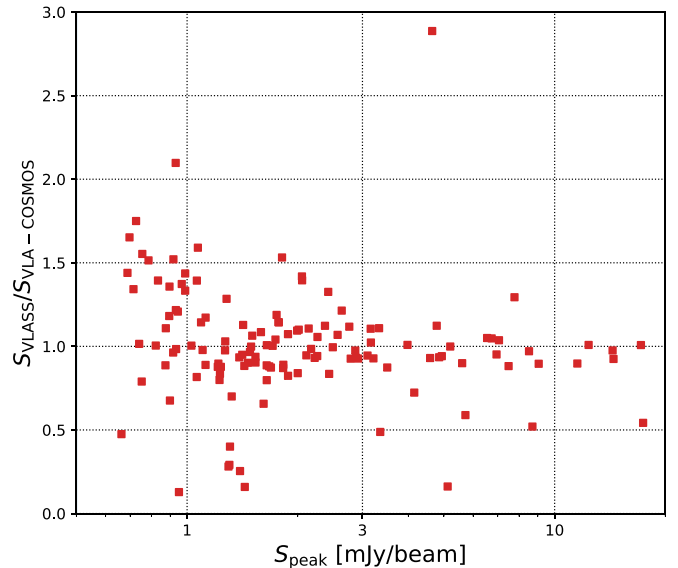


**Figure 5.** Comparison of VLASS flux measurements to the 3 GHz VLA-COSMOS measurements for the 131 matched components in the  $2 \text{ deg}^2$  of the COSMOS field.

VLASS. This sample contains 33 components with a peak VLASS brightness greater than  $3 \text{ mJy beam}^{-1}$ , and for these the median value of  $S_{\text{VLASS}}/S_{\text{VLA-COSMOS}}$  is 0.95 with a standard error of 0.07. Below about  $3 \text{ mJy beam}^{-1}$  there is substantial scatter in the ratio of measured flux densities between VLASS and VLA-COSMOS.

#### 3.2.2. Comparisons with Multiband Radio Data

Given the limited available  $\nu \sim 3$  GHz data with which to compare our catalog, we adopt a method similar to that used by Sabater et al. (2021) in order to estimate the reliability of our flux density measurements. This approach determines the distribution of flux density ratios for matched components between the survey being calibrated and a reference survey at a number of different frequencies. A power law can then be fit to the average flux density ratio as a function of frequency, with the intercept at the frequency of the survey being calibrated used to determine the flux density accuracy. As the VLASS footprint covers  $\sim 80\%$  of the sky, there are a number of overlapping wide-field continuum surveys that can be used in this way.

We compare our data with TGSS at 150 MHz, the Westerbork Northern Sky Survey (WENSS; Rengelink et al. 1997) at 330 MHz, the Sydney University Molonglo Sky Survey (SUMSS; Bock et al. 1999; Mauch et al. 2003) at 840 MHz, and FIRST at 1.4 GHz. As all these surveys have different angular resolutions and effective depths,<sup>8</sup> care must be taken when matching components. For instance, WENSS has an angular resolution of  $54'' \text{ csc}(\text{decl.})$ , and a single WENSS component could easily be observed as multiple components in VLASS. Therefore, to qualify as a matched component, we require the distance to the nearest neighboring VLASS component to be greater than half the angular resolution of the comparison survey, using the *isolation radius* given in

<sup>8</sup> Defined as the noise level when accounting for observing frequency assuming a typical spectral index of  $-0.7$ ; higher (lower) effective noise levels imply shallower (deeper) surveys.

**Table 1**  
Parameters Used when Matching Comparison Surveys with VLASS for Flux Calibration

Survey	$\nu$ (MHz)	Isolation Radius (arcseconds)	$\Psi_{\max}$ (arcseconds)	$S_{\min}$ (mJy)	$N$
TGSS	150	14	30	60	806
	330	54	0	20	1636
	843	43	10	10	1747
	1400	2.7	1	2	6189
	3000	...	0.5	3	...

**Note.** The frequency ( $\nu$ ) of the survey in MHz, the minimum angular distance to the nearest neighbor for the matched VLASS component in arcseconds, and the minimum flux density of components from that survey used in mJy are listed for each survey. The number of matched components for which the VLASS-to-comparison-survey flux density ratios are used to calibrate the VLASS flux is given in the last column.

Table 1. As the elliptical beam geometry varies with decl. for TGSS, WENSS, and SUMSS, the poorest possible resolution in the overlap with VLASS is assumed when defining this isolation limit for these surveys.

Only unresolved or barely resolved components are matched to one another in this calibration. For VLASS, we consider components with a deconvolved angular size,  $\Psi$ , of less than  $0''.5$  to be suitable here. The maximum angular sizes of components we use from the comparison surveys are listed in Table 1, and for FIRST and SUMSS these are based on the cataloged deconvolved sizes. The WENSS catalog provides the Gaussian fitted sizes (i.e., including the beam size) for resolved components and lists a “zero” size where the ratio of peak and integrated flux density is indicative that the component is unresolved (Rengelink et al. 1997). It is these unresolved WENSS components that we include in our analysis. TGSS only provides a fitted component size and does not highlight likely unresolved components, so we only consider TGSS components with a fitted angular size smaller than  $30''$  in this analysis.

The appropriate samples of isolated VLASS components are then cross-matched with their respective comparison surveys. As TGSS, WENSS, and SUMSS have substantially poorer angular resolutions than VLASS, we use a search radius of  $5''$  when cross-matching these surveys with VLASS. For FIRST, which has an angular resolution ( $5''.4$ ) that is more comparable to that of VLASS, a search radius of  $2''.5$  is used.

All of the comparison surveys are at a lower frequency than VLASS; comparing to a survey with a greater effective depth (e.g., FIRST) will be biased by components with flat- or inverted-spectrum sources. Comparisons with lower effective depth surveys (e.g., WENSS) will be biased toward components with very steep negative spectral indices. This effect can be seen in the curvature at the low ends of the flux density comparisons for VLASS, WENSS, and FIRST shown in Figure 6. To eliminate this bias, we select only components with a spectral index,  $\alpha$ , in the range  $-1.5 < \alpha < +0.5$ , which would be detectable in both VLASS and the comparison survey. Explicitly, this is achieved by satisfying

$$S_{\text{VLASS}} > \frac{S_{\min, \text{comparison}}^2}{S_{\text{comparison}}} \times \left( \frac{3 \text{ GHz}}{\nu_{\text{comparison}}} \right)^{+0.5}, \quad (1)$$

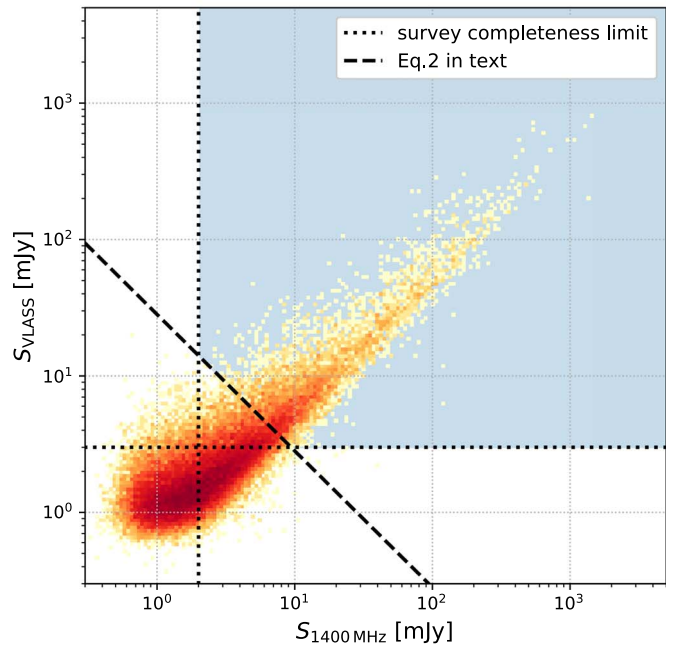
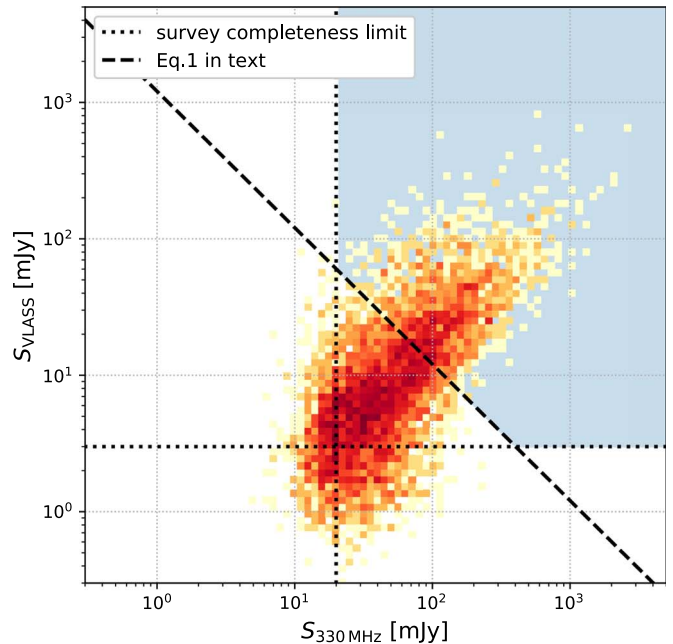


**Figure 6.** Examples of VLASS flux densities compared to two of the comparison surveys. The top panel shows the comparison with a shallower survey, WENSS ( $\nu \sim 330$  MHz), and the bottom panel shows the comparison with the deeper survey, FIRST ( $\nu \sim 1400$  MHz). The red/yellow density plots show the flux densities in VLASS and the comparison survey for all cross-matched compact components. The black dashed lines show the minimum flux density used as a completeness limit for each survey, while the solid black line shows the cutoff we apply to prevent the different effective survey depths biasing our flux calibration. For WENSS this is based on Equation (1), and for FIRST this is based on Equation (2). The light-blue shaded region above and to the right of the three black lines highlights the components selected for use in our VLASS flux calibration.

when the comparison survey is effectively shallower (TGSS, WENSS, and SUMSS), and by

$$S_{\text{VLASS}} > \frac{(3 \text{ mJy})^2}{S_{\text{comparison}}} \times \left( \frac{\nu_{\text{comparison}}}{3 \text{ GHz}} \right)^{-1.5}, \quad (2)$$

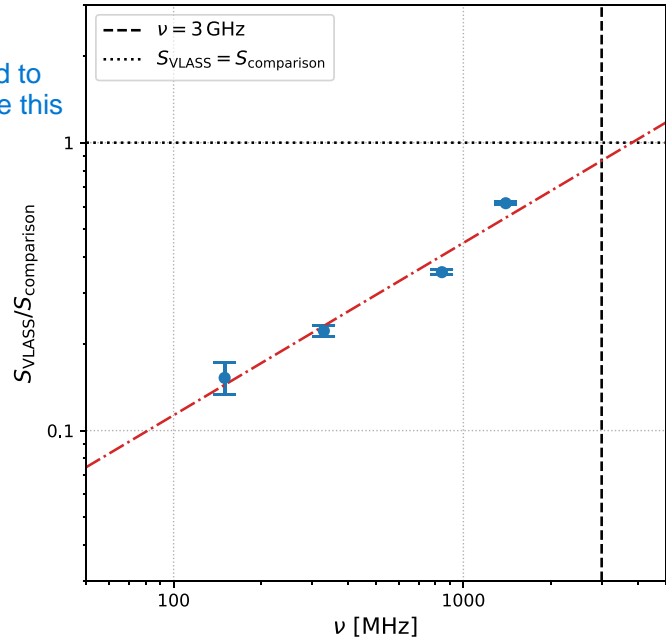


**Figure 7.** The median ratio of VLASS to comparison survey flux density for cross-matched components as a function of comparison survey frequency. Error bars represent the standard error. Four comparison surveys are used here: TGSS at 150 MHz, WENSS at 330 MHz, SUMSS at 840 MHz, and FIRST at 1400 MHz. The red dashed-dotted line shows the best fit to the data, a power law with a slope of 0.6, from which we extrapolate  $S_{\text{VLASS}}/S_{3 \text{ GHz}} = 0.87$ . The black dotted line shows unity for the ratio of VLASS to comparison flux densities, and the black dashed line marks  $\nu = 3 \text{ GHz}$ .

when the comparison survey is effectively deeper (FIRST).  $S_{\text{VLASS}}$  is the VLASS flux density of the component,  $S_{\text{comparison}}$  is the flux density of the component in the comparison survey,  $S_{\min, \text{comparison}}$  is the completeness limit of the comparison survey (see Table 1),  $\nu_{\text{comparison}}$  is the comparison survey frequency, and the completeness limit of VLASS is taken to be 3 mJy. This selection is shown by the light-blue shaded regions in Figure 6 for WENSS and FIRST.

For the selected components we determine the median ratio of flux densities between VLASS and the comparison survey, and these are shown as a function of frequency in Figure 7. We fit a power law to these data points with a slope of 0.6 in order to extrapolate the expected flux density ratio between VLASS and benchmark 3 GHz measurements and thus quantify the typical underestimation of flux density measurements in our catalog. From this we determine  $S_{\text{VLASS}} = 0.87 S_{3 \text{ GHz}}$ . To compensate for this typical underestimate, we scale all the VLASS flux density measurements by 1/0.87 throughout the rest of this work. This correction is not applied to our catalog, and anyone making use of these data is advised to apply the flux density correction themselves.

### 3.3. Astrometry

Early investigations by NRAO into the epoch 1.1 *Quick Look* imaging showed issues with respect to the astrometric accuracy of the *Quick Look* images (Lacy et al. 2019). Comparisons with Gaia DR2 (Gaia Collaboration et al. 2016, 2018) showed the VLASS component positional accuracy to be limited to  $\sim 1''$ , improving to  $\sim 0''.5$  at  $\text{decl.} > -20^\circ$ . These limitations to the VLASS astrometry are attributable to two factors. First, the rapid processing technique

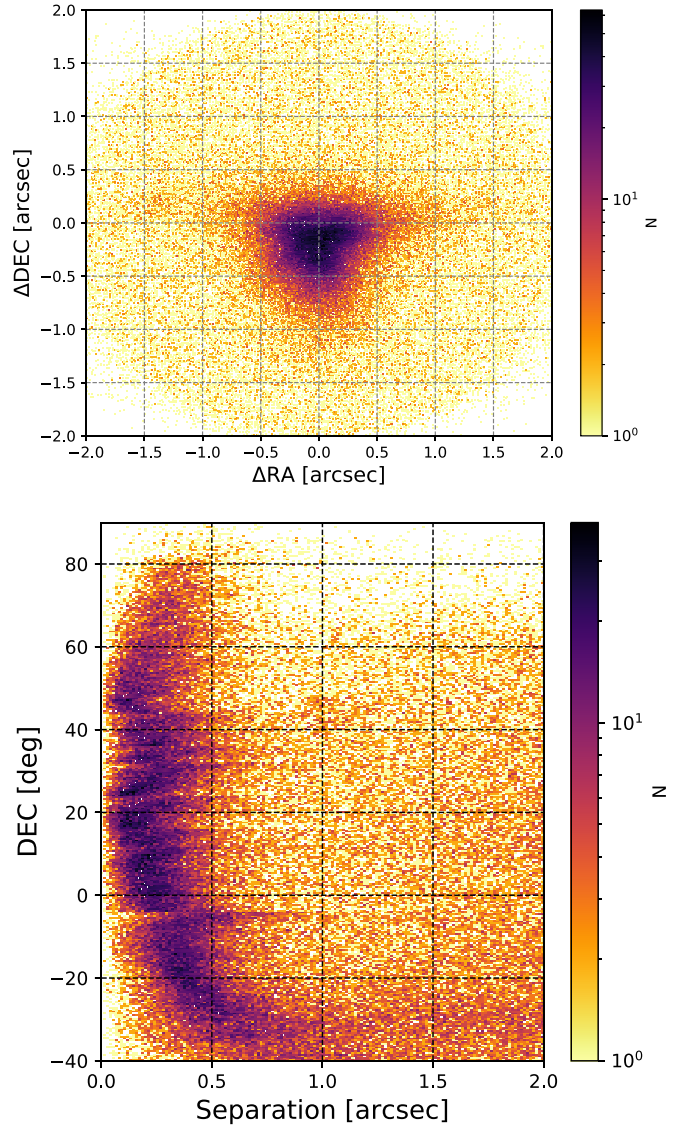


**Figure 8.** The positional offsets of Gaia and VLASS sources separated by less than  $2''$ . The top panel shows the offset in terms of R.A. and decl. Here  $\Delta x = x_{\text{Gaia}} - x_{\text{VLASS}}$ , where  $x = \text{R.A.}, \text{decl.}$  While the peak of  $\Delta\text{R.A.}$  is close to 0,  $\Delta\text{decl.}$  peaks at around  $-0''.25$ , showing the VLASS *Quick Look* imaging astrometric errors to be dominated by offsets in decl. The bottom panel shows the separation,  $\sqrt{\Delta\text{R.A.}^2 + \Delta\text{decl.}^2}$ , between VLASS and Gaia sources as a function of decl. At  $\text{decl.} < -20^\circ$  the peak of the positional offset tends to higher separations, indicating poorer astrometry at these declinations.

employed fails to account for the  $w$ -term in the interferometer equation (Smirnov 2011a, 2011b). The impact of this is to distort the VLASS point-spread function away from the phase center, resulting in positional offsets in detections. Second, the pixels in the *Quick Look* images are  $1''$  compared to a typical VLASS beam size of  $2''.5$ . Thus, the pixels in the *Quick Look* do not adequately sample the beam, and this may contribute to the positional uncertainty.

Comparing our catalog with Gaia DR2, we confirm NRAO’s findings in this regard. In Figure 8 we show the positional offset explicitly as  $\Delta\text{R.A.}$  and  $\Delta\text{decl.}$ , where  $\Delta x = x_{\text{Gaia}} - x_{\text{VLASS}}$  for  $x = \text{R.A.}, \text{decl.}$  The separation between VLASS components and Gaia sources is strongly peaked owing to genuine associations. If the astrometry for both surveys were perfect, one would expect the peak from genuine associations to occur at  $\theta = 0''$ , but we observe that the decl. offset peaks at

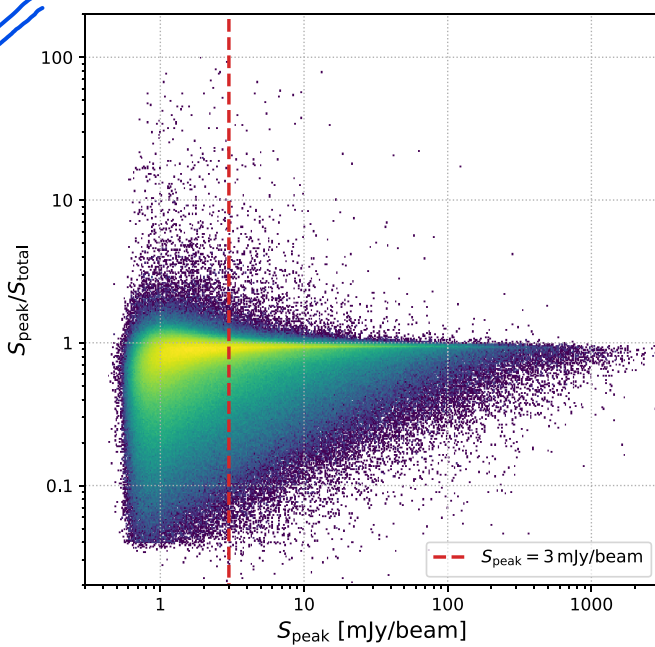


**Figure 9.** The ratio of peak brightness to total flux density as a function of peak brightness for the  $\sim 1.9 \times 10^6$  components in our VLASS catalog with  $Quality\_flag == (0|4)$ ,  $Duplicate\_flag < 2$ , and  $S\_Code \neq "E"$ . The red dashed line shows the brightness level of  $3 \text{ mJy beam}^{-1}$  used in this work to select components with the most reliable flux density measurements (see also Section 3.2). The large population of components with  $S_{\text{peak}}/S_{\text{total}} < 1$  represents well-resolved VLASS components. Components with  $S_{\text{peak}}/S_{\text{total}} > 1$  are unresolved components, and  $\sim 8\%$  of these are spurious in VLASS *Quick Look* images.

$\Delta\text{decl.} \approx -0.^{\circ}25$ . The offset in R.A. is minimal with a median of  $\Delta\text{R.A.} \approx 0$ . In agreement with the findings in Lacy et al. (2019), we also confirm that the positional offset is worse at  $\text{decl.} > +60^\circ$  and  $\text{decl.} < 0^\circ$ , with the separations between VLASS and Gaia sources mostly being  $< 0.^{\circ}5$  at  $\text{decl.} > -20^\circ$  (see Figure 8).

### 3.4. Data Selection

In Section 2.3 we detailed the efforts we have undertaken to identify the spurious detections that are present in our VLASS *Quick Look* catalog. While a selection based on  $Quality\_flag == 0$  provides a sample containing the most reliable measurements, this may not be a complete sample and thus will hinder a statistical characterization of the survey. In particular, the choice to exclude components where  $Peak\_flux > Total\_flux$  will remove a substantial number of real detections that are unresolved by VLASS, in addition to removing low-S/N false-positive detections.

To retain this population of unresolved components for the statistics presented in this paper, with the acceptance of source contamination by false-positive detections at lower S/N, we select components from our catalog with  $Quality\_flag == (0|4)$ ,  $Duplicate\_flag < 2$ , and  $S\_Code \neq "E"$ . This sample of 1,880,195 components represents the  $\sim 1.7 \times 10^6$  selected by the original, higher-fidelity criteria outlined in Section 2.3 ( $Duplicate\_flag < 2$  and  $Quality\_flag == 0$ ), with the addition of fitted components (i.e., not “empty islands”) where  $Peak\_flux > Total\_flux$ . The distribution of the ratio of peak to total flux density as a function of peak brightness for these components is shown in Figure 9.

In order to quantify the impact of potential spurious detections arising from the population of  $Quality\_flag == 4$

components, i.e., those with  $S_{\text{peak}} > S_{\text{total}}$  but otherwise unflagged in our catalog, we visually inspect a random sample of 100 of these components. Here we find that  $92^{+2}_{-4}\%$ <sup>9</sup> are clearly real detections. As the  $Quality\_flag == 4$  components account for 10% of the sample, this suggests a contamination level of  $< 1\%$  spurious detections. Moreover, for components with  $S_{\text{peak}} > 3 \text{ mJy beam}^{-1}$  used for most of the scientific analysis in this work (see Section 3.2.1), only 6% have  $Quality\_flag == 4$ , suggesting a contamination level of  $< 0.5\%$  at this brightness level. Throughout the rest of this work we use these  $\sim 1.9 \times 10^6$  components with  $Quality\_flag == (0|4)$ ,  $Duplicate\_flag < 2$ , and  $S\_Code \neq "E"$  as our primary sample. Many of the analyses presented are further restricted to the 615,045 components with  $S_{\text{peak}} > 3 \text{ mJy beam}^{-1}$ , where the reliability in the flux density measurements is best characterized (see Section 3.2).

## 4. Spectral Index and Curvature

### 4.1. The VLASS/FIRST Spectral Index Distribution

In the remainder of this work, we use the catalog of components from *Quick Look* images to explore the scientific potential of VLASS. The availability of wide-field  $\nu \sim 3 \text{ GHz}$  observations at similar depths to previous surveys at  $1.4 \text{ GHz}$  lends itself to determining the distribution of spectral indices at these frequencies. For this we cross-match VLASS and FIRST components within  $2.^{\circ}5$  of each other (85% are within  $1.^{\circ}$ ), where the cross-match radius is based on the typical VLASS beam size. As in Section 3.2.2, we require the VLASS component to be isolated in order to prevent the flux from the poorer resolution FIRST observations being split across multiple VLASS components (see also Section 6.3). To enable further cross-matching with LoTSS, which allows us to explore the spectral curvature of these objects in Section 4.2, we require the distance to the nearest neighbor in VLASS to be greater than  $3.^{\circ}$ —half of the LoTSS beam size ( $6.^{\circ}$ ; Shimwell et al. 2019). So as to limit issues relating to VLASS missing flux from extended low surface brightness regions, only relatively small FIRST components, those with deconvolved sizes of  $< 10.^{\circ}$ , are included in this sample. We then determine the spectral index for  $> 500,000$  VLASS components using their VLASS and FIRST total flux density measurements.

In Figure 10 we show the two-point 1.4–3 GHz spectral index distribution, which peaks at  $\alpha = -0.57$  and has a median of  $\alpha = -0.39$ , flatter than the typical value of  $\alpha \sim -0.7$  one would expect based on previous works (e.g., Condon et al. 2002; Best et al. 2005; de Gasperin et al. 2018). We showed in Figure 5 that VLASS flux densities below  $\sim 3 \text{ mJy}$  are unreliable, and we thus limit our sample of matched VLASS and FIRST components to those with a peak brightness higher than  $3 \text{ mJy beam}^{-1}$ . Doing this, we find that the distribution peaks at  $\alpha = -0.71$ , in line with canonical values for the spectral indices of radio sources (see Figure 10). Setting an even higher limit on the minimum flux density of the sample of  $S > 10 \text{ mJy beam}^{-1}$ , the peak of the distribution is located at  $\alpha = -0.72$  (see Table 2).

Although our spectral index distribution is cleaner at  $S_{3 \text{ GHz}} > 3 \text{ mJy beam}^{-1}$ , we note that the skew to flatter spectral indices when including components below the brightness threshold (see the top panel of Figure 10) may be a real effect. If this observation were to hold up with higher-quality

<sup>9</sup> Errors are assumed to be binomial based on Cameron (2011).

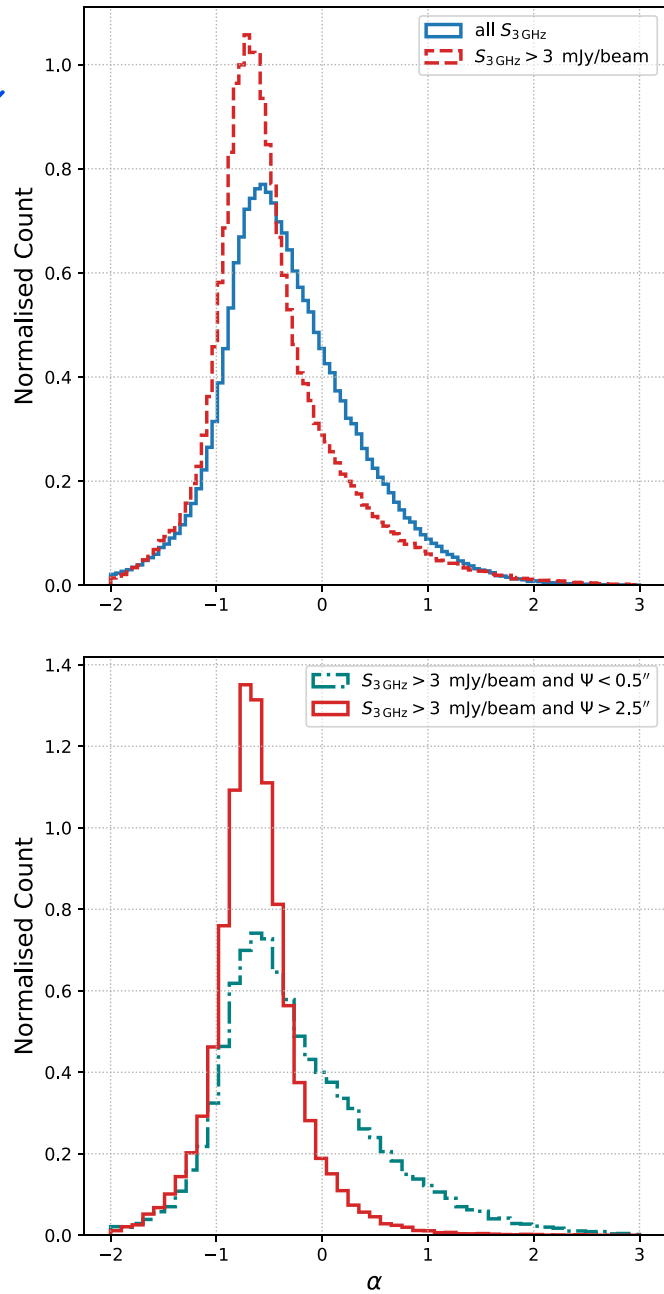


**Figure 10.** Normalized distributions of the spectral index,  $\alpha$ , for VLASS components associated with FIRST components with deconvolved sizes of less than  $10''$ . The top panel compares the spectral index distributions for VLASS components over the full range of detected flux densities (blue solid line) to those with  $S_{3\text{ GHz}} > 3 \text{ mJy beam}^{-1}$  (red dashed line). The bottom panel compares components with deconvolved sizes greater than  $2.5''$  (red solid line) to those smaller than  $0.5''$  (blue-green dotted-dashed line). We follow the convention that  $S \propto \nu^\alpha$ , and the spectral index is calculated using the total flux densities from the FIRST and VLASS catalogs.

data, it could support the observations of, e.g., Prandoni et al. (2006), Owen & Morrison (2008), and Whittam et al. (2013) of a flattening of spectral indices at flux densities of  $\sim 1 \text{ mJy}$ , likely due to an increase in radio core dominance at low radio luminosities (Whittam et al. 2017). The future availability of cleaner VLASS *Single Epoch* images will allow reliable measurements of flux densities at this level, and the stacked three-epoch VLASS images will allow testing of this hypothesis using components with  $\lesssim 1 \text{ mJy}$ .

**Table 2**  
Peak and Median Values of the Spectral Index Distributions for VLASS Components Matched to FIRST Components with a Deconvolved Angular Size,  $\Psi$ , less than  $10''$

Component Subset	$N$	Peak $\alpha$	Median $\alpha$
All	533,739	-0.57	-0.39
$S_{3\text{ GHz}} > 3 \text{ mJy beam}^{-1}$	182,638	-0.71	-0.58
$S_{3\text{ GHz}} > 10 \text{ mJy beam}^{-1}$	57,181	-0.72	-0.65
$\Psi < 0.5''$ and $S_{3\text{ GHz}} > 3 \text{ mJy beam}^{-1}$	33,279	-0.66	-0.38
$\Psi > 2.5''$ and $S_{3\text{ GHz}} > 3 \text{ mJy beam}^{-1}$	40,621	-0.70	-0.65
WISE counterpart, $\Psi < 0.55''$ and $S_{3\text{ GHz}} > 3 \text{ mJy beam}^{-1}$	22,235	-0.63	-0.27
No WISE counterpart, $\Psi < 0.55''$ and $S_{3\text{ GHz}} > 3 \text{ mJy beam}^{-1}$	5769	-0.81	-0.59

**Note.** The number of components in each data set is given by  $N$ .

Notably, even when applying a cut on minimum flux density, the spectral index distributions for VLASS components have a skew toward flatter values. A potential explanation for this is the high resolution of VLASS results in radio lobes being resolved as separate components to their cores. To investigate the impact of resolved radio cores on the VLASS/FIRST spectral index distribution, we split our sample into likely compact and extended components with a peak brightness of  $S_{3\text{ GHz}} > 3 \text{ mJy beam}^{-1}$ . We define compact as having  $\Psi < 0.5''$  and extended as having  $2.5'' < \Psi < 10''$  (and thus larger than a typical VLASS beam). Here we find that the spectral index distribution for compact components peaks at  $\alpha = -0.66$  with a median of  $\alpha = -0.38$ , compared to  $-0.70$  and  $-0.65$ , respectively, for extended components (see Figure 10).

Furthermore, we can improve the identification of radio cores by requiring that a compact component is spatially coincident with an infrared or optical source. To this end we cross-match our sample with the AllWISE catalog (Cutri et al. 2013), based on observations from the Wide-field Infrared Survey Explorer telescope (WISE; Wright et al. 2010). If a component has an AllWISE detection in the W1 band ( $\lambda \sim 3.4 \mu\text{m}$ ) within  $2.5''$ , we associate the radio component and the infrared source with one another. Conversely, we consider a radio component to not have an AllWISE match if there is no W1-band detection within  $10''$ . For compact components with an AllWISE match, the spectral index distribution peaks at  $\alpha = -0.63$  and has a median of  $\alpha = -0.27$ . Where a compact component is not associated with an AllWISE match, the spectral index distribution peaks at  $\alpha = -0.81$ , with a median of  $\alpha = -0.59$ . Although this shows that radio cores contribute to the flatter spectrum bias of the VLASS/FIRST spectral index distribution, no account is taken in determining the spectral indices of potential for radio variability that may be present in a few percent of radio sources (e.g., Carilli et al. 2003; Mooley et al. 2016; Nyland et al. 2020). The availability of second-epoch VLASS observations will enable the impact of radio variability on this distribution to be quantified. The peak and median values of all the spectral index distributions analyzed here, including those with and without an AllWISE counterpart, are listed in Table 2.

#### 4.2. Spectral Curvature between 150 MHz and 3 GHz

The availability of the first data release of LoTSS (DR1; Shimwell et al. 2019) allows for comparisons of our catalog

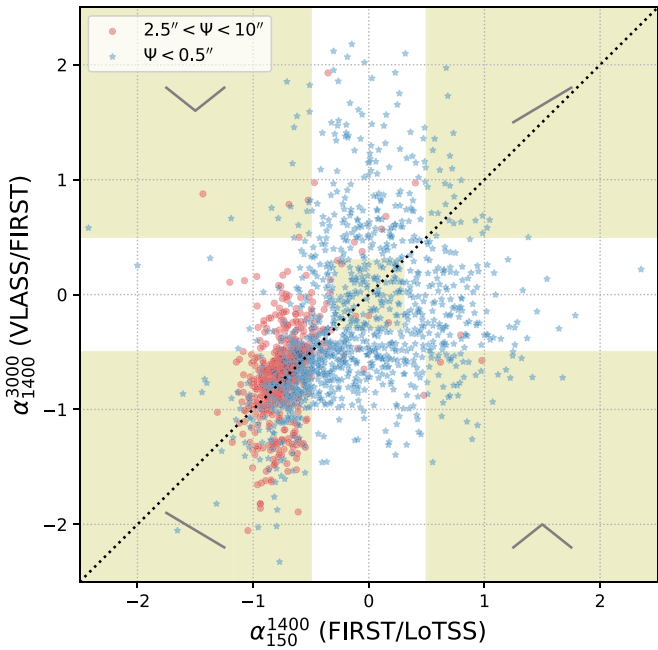


**Figure 11.** Radio color–color plot for our VLASS components matched with components from both FIRST and LoTSS, where the determined spectral indices are based on the component’s total flux density from each survey. Blue stars represent compact components ( $\Psi < 0''.5$ ), while extended components ( $2''.5 \leq \Psi \leq 10''$ ) are shown as red circles. The  $x$ -axis gives the spectral index determined from FIRST (1400 MHz) and LoTSS (150 MHz), and the  $y$ -axis shows the spectral index based on VLASS (3000 MHz) and FIRST measurements (1400 MHz). The black dotted line on both panels shows  $\alpha_{150}^{1400} = \alpha_{1400}^{3000}$ . The shaded yellow regions show the definitions used in this work for concave-spectrum (upper left), normal-spectrum (lower left), inverted-spectrum (upper right), and GPS (lower right) sources. The gray line in each of these shaded corners shows the representative spectral shape (note that spectral curvature will increase away from the black dotted line). The shaded yellow region at the center defines sources we consider as flat-spectrum.

with deep (rms  $\sim 70 \mu\text{Jy beam}^{-1}$ ), high-resolution ( $\sim 6''$ ), low-frequency ( $\nu \sim 150 \text{ MHz}$ ) observations over  $\sim 400 \text{ deg}^2$ . LoTSS DR1 lies within the FIRST footprint, allowing us to match our cross-matched VLASS/FIRST components with LoTSS, again using a  $2''.5$  search radius, providing flux density measurements in three radio bands for these components. We find  $\sim 17,000$  VLASS components with observations from both FIRST and LoTSS and a FIRST deconvolved size smaller than  $10''$ , 5497 of which have  $S_{3 \text{ GHz}} > 3 \text{ mJy beam}^{-1}$ .

As in Section 4.1, we split our sample of radio components into *compact* (deconvolved size,  $\Psi, < 0''.5$ ,  $n = 1205$ ) and *extended* ( $\Psi > 2''.5$ ,  $n = 645$ ) using the deconvolved major-axis size of the VLASS component. As in Section 4.1, the spectral indices are determined based on the cataloged total flux densities of the components. Comparing the low- (150 MHz  $\lesssim \nu \lesssim 1,400$  MHz) and high-frequency (1400 MHz  $\lesssim \nu \lesssim 3000$  MHz) spectral indices of these components demonstrates their spectral curvature and is shown on a radio “color–color” plot in Figure 11. Most components possess normal radio spectra, with the highest density of both compact and extended components at  $-1 \lesssim \alpha_{1400}^{3000} \approx \alpha_{150}^{1400} \lesssim -0.5$ . A population of the extended components shows clear spectral curvature, a feature often being associated with older radio lobes (Kharb et al. 2008; Harwood et al. 2017). The radio colors of compact components show substantial scatter, with radio colors displaying inverted spectra (positive spectral index at low and high frequency), flat spectra (spectral index  $\sim 0$  at low and high

frequency), gigahertz-peaked spectra (GPS; positive low-frequency and negative high-frequency spectral indices; O’Dea 1998; O’Dea & Saikia 2021), and concave spectra (negative low-frequency and positive high-frequency spectral indices). These distinct populations are highlighted in Figure 11. Some of the scatter in the radio color–color parameter space will be driven by radio variability, the impact of which will be quantifiable with the forthcoming availability of VLASS epoch 2 observations.

#### 4.3. Infrared Colors of Compact Radio Sources with Differing Spectral Shapes

Considering point-like radio components as individual compact sources can have tangible scientific benefit, allowing us to cross-match with multiwavelength observations and provide insights into the properties of their host galaxies. To this end we use the cross-match between VLASS and AllWISE described in Section 4.1 to obtain infrared magnitudes for the likely hosts of these compact sources. From this cross-match we then select five samples of compact sources exhibiting different radio spectra:

1. GPS sources with  $\alpha_{150}^{1400} > +0.5$  and  $\alpha_{1400}^{3000} < -0.5$ : 41 objects, 22 with AllWISE matches;
2. inverted-spectrum sources having  $\alpha_{150}^{1400} > +0.5$  and  $\alpha_{1400}^{3000} > +0.5$ : 25 objects, 18 with AllWISE matches;
3. flat-spectrum sources with  $-0.3 < \alpha_{150}^{1400} < +0.3$  and  $-0.3 < \alpha_{1400}^{3000} < +0.3$ : 129 objects, 94 with AllWISE matches;
4. concave-spectrum sources with  $\alpha_{150}^{1400} < -0.5$  and  $\alpha_{1400}^{3000} > +0.5$ : 17 objects, 14 with AllWISE matches; and
5. for reference, normal-spectrum sources having  $\alpha_{150}^{1400} < -0.5$  and  $\alpha_{1400}^{3000} < -0.5$ : 246 objects, 147 with AllWISE matches.

In Figure 12 we show the WISE colors (W1 [ $3.4 \mu\text{m}$ ]–W2 [ $4.3 \mu\text{m}$ ] and W2–W3 [ $12 \mu\text{m}$ ]) of the samples defined above. We then classify the host galaxies as either early or late type using the criteria of Jarrett et al. (2017), or as active galactic nuclei (AGN) based on Jarrett et al. (2011).

Infrared colors associated with early-type galaxies are relatively uncommon among our sample—potentially the result of only including unresolved radio sources—accounting for  $3.4_{-0.9}^{+2.2}\%$  of normal-spectrum,  $5.3_{-1.5}^{+3.3}\%$  of flat-spectrum, and  $7.1_{-2.3}^{+13.2}\%$  of concave-spectrum sources. None of the 26 GPS sources in our sample have WISE colors expected of early-type galaxies. For inverted-spectrum sources, however,  $16.7_{-5.4}^{+12.1}\%$  have WISE colors associated with early-type hosts. Unfortunately, the small size of our sample (17 objects) prevents any statistically significant conclusions from being drawn here, but we note that where inverted-spectrum sources are associated with early-type colors, these colors are within half a magnitude of the Jarrett et al. (2017) early-/late-type segregation of the WISE color–color space.

More generally, the WISE colors of our sample of compact radio sources are split between being consistent with late-type and AGN hosts. Late-type hosts account for 43%–57% of compact radio sources (depending on spectral shape), while 35%–45% of sources have AGN-like WISE colors. The fractions of normal-spectrum, GPS, inverted-spectrum, flat-spectrum, and concave-spectrum sources having WISE colors associated with AGN, late-type, and early-type galaxies are

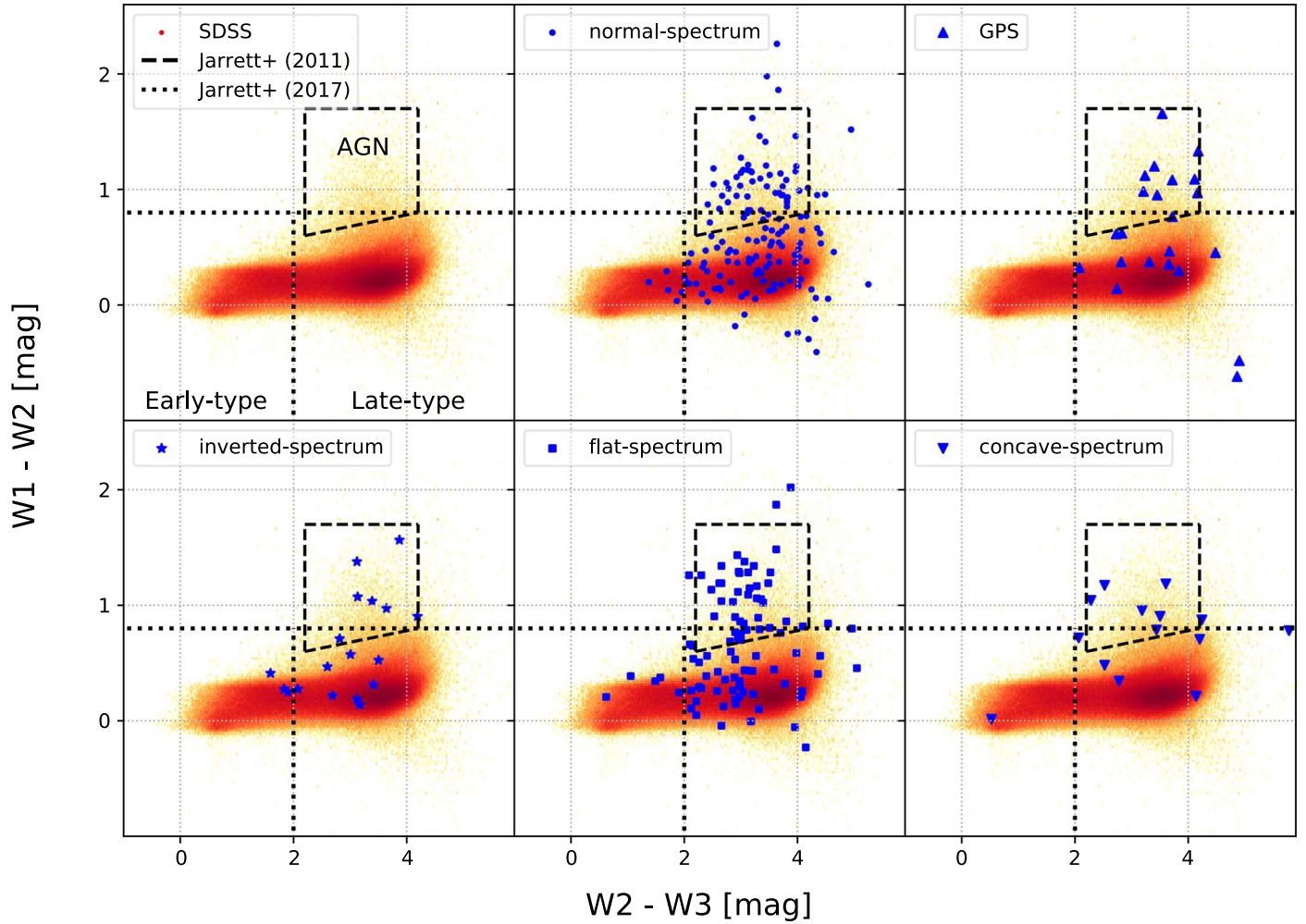


**Figure 12.** WISE color–color diagrams for compact radio sources with different spectral properties. We show five types of radio source here: normal-spectrum sources (blue circles, top middle panel), GPS sources (blue triangles, top right panel), inverted-spectrum sources (blue stars, bottom left panel), flat-spectrum sources (blue square, bottom middle panel), and concave-spectrum sources (inverted blue triangles, bottom right panel). The WISE color–color distribution of galaxies in SDSS is shown in red for reference (and for clarity on its own in the top left panel). The  $x$ -axis shows the  $W1 - W2$  color, and  $W2 - W3$  is shown on the  $y$ -axis. The black dashed line shows the quasar/AGN region defined by Jarrett et al. (2011), and the black dashed line marks out the regions of color–color space occupied by early- (left) and late-type galaxies (right; Jarrett et al. 2017).

explicitly given in Table 3. For comparison with the general galaxy population, we also show the WISE colors of the MPA/JHU sample from the seventh data release of the Sloan Digital Sky Survey (SDSS; York et al. 2000; Kauffmann et al. 2003; Abazajian et al. 2009) in Figure 12, and the fractions of each color classification (AGN, late type, or early type) are given in Table 3. It is worth noting, however, that while the host of a radio source may have WISE colors associated with star-forming disk galaxies as defined by Jarrett et al. (2017), that in and of itself does not mean that star formation is responsible for the radio emission as opposed to an AGN.

Despite the clear advantages of matching the VLASS, FIRST, and LoTSS catalogs, the observations were not made simultaneously. Thus, there will exist contamination from sources exhibiting radio variability. Tackling this is beyond the scope of the work presented here, which acts as a small-scale proof of concept. However, the future advent of multiepoch observations from VLASS will be invaluable in identifying such detections. Additionally, as more data are released by LoTSS, the footprint over which such radio color–color data are available will increase beyond the  $\sim 400 \text{ deg}^2$  of the first LoTSS data release utilized here. Eventually, such a

**Table 3**  
Percentage and Binomial Errors of Fractions of Compact Sources with IR Counterpart Classifications as Defined by Jarrett et al. (2011, 2017) Based on Their WISE Colors (See Also Figure 12)

Sample	AGN (%)	Late Type (%)	Early Type (%)
SDSS	$0.9^{+0.01}_{-0.01}$	$75.4 \pm 0.06$	$23.6 \pm 0.05$
Normal-spectrum	$35.4^{+4.1}_{-3.7}$	$57.1^{+4.0}_{-4.2}$	$3.4^{+2.2}_{-0.9}$
GPS	$45.5^{+10.6}_{-9.8}$	$54.5^{+9.8}_{-10.6}$	$0.0^{+7.7}_{-0.0}$
Inverted-spectrum	$38.9^{+12.1}_{-9.8}$	$44.4^{+11.7}_{-10.6}$	$16.7^{+12.1}_{-5.4}$
Flat-spectrum	$41.5^{+5.2}_{-4.9}$	$48.9 \pm 5.1$	$5.3^{+3.3}_{-1.5}$
Concave-spectrum	$42.9^{+13.3}_{-11.5}$	$42.9^{+13.3}_{-11.5}$	$7.1^{+13.2}_{-2.3}$

VLASS/FIRST/LoTSS color–color map will be limited only by the  $\sim 10,000 \text{ deg}^2$  of the FIRST footprint.

## 5. Euclidean Normalized Source Counts

For the first time wide-field coverage of the sky at 3 GHz down to mJy sensitivities is made available through these data. Thus, this presents a prime opportunity to quantify the

Euclidean normalized (i.e., normalized to the assumption of a geometrically flat and steady-state universe) 3 GHz source counts,  $dN/dS$ , at this depth. In order to do this, we must account for several complicating factors.

First, in Figure 4 we demonstrate that the depth of the *Quick Look* imaging is distinctly nonhomogeneous. This will have an impact on the effective survey footprint over which faint sources can be detected. That is to say that while a 1 mJy component may be readily detected in a relatively deep part of the survey, in one of the shallower regions (e.g., the Galactic plane which is shown in Figure 4 to be particularly noisy) that component may not be detected. The dominant source of noise variance in the *Quick Look* images is due to observing tile edge effects—the distinctly higher noise at the edge of a VLASS tile. To estimate the impact of this, we compare the peak brightness distributions of components more than  $0.^{\circ}2$  from a tile edge (and therefore not impacted by tile edge effects) with the full VLASS component peak brightness distribution. Bin-wise dividing the not-edge peak brightness distribution by the full sample peak brightness distribution provides the average completeness (and thus incompleteness) as a function of peak brightness due to tile edge effects,  $p_{\text{edges}}(S)$ . Additionally, the average noise in a particular image can be impacted by the presence of bright radio components. By taking  $5\times$  the mean image rms as the limiting flux density for a component to be detected in an image, we can estimate the sensitivity distribution of the *Quick Look* images. We can combine the distribution of image rms with the completeness due to tile edge effects to give a probability distribution,  $P(S)$ , of a component of flux density  $S$  being detected across the survey footprint, i.e.,  $P(S) = p_{\text{edges}}(S) \times p_{\text{imdepth}}(S)$ , where  $p_{\text{edges}}(S)$  is the contribution from tile edge effects and  $p_{\text{imdepth}}(S)$  is the contribution from varying image effective depth. At  $S_{\text{peak}} = 3 \text{ mJy beam}^{-1}$  the sample completeness is 99.8%, whereas at the  $1 \text{ mJy beam}^{-1}$  level the completeness of the catalog is 67%. The effective survey footprint as a function of component brightness is then estimated by  $P(S) \times A_{\text{VLASS}}$ , where  $A_{\text{VLASS}}$  is the total observed footprint of the survey.

The second complication in deriving the VLASS *Quick Look*  $dN/dS$  is due to the fact that individually detected radio components are often resolved parts of larger structures that make up a distinct source. To counter this, and for consistency with previous works, we adopt the approach that most radio components within  $50''$  are related (Oosterbaan 1978; Windhorst et al. 1985; White et al. 1997). Hence, for all components within  $50''$  of one another, their integrated flux densities are summed and they are treated as a single source.

The VLASS *Quick Look*  $dN/dS$ , corrected for  $P(S)$ , is shown in Figure 13 alongside VLA-COSMOS—the previously largest available 3 GHz data set. While VLA-COSMOS probes deeper than VLASS, there is overlap in the flux density range covered by these surveys between  $1 \text{ mJy} \lesssim S \lesssim 10 \text{ mJy}$ , and above  $\sim 3 \text{ mJy}$  the VLASS  $dN/dS$  is shown to be consistent with the  $dN/dS$  from VLA-COSMOS. To compare with a radio survey covering a similar flux density range, we additionally compare the VLASS  $dN/dS$  to the FIRST  $dN/dS$  (also shown in Figure 13) by extrapolating the VLASS flux measurements to 1.4 GHz assuming a spectral index of  $\alpha = -0.71$ . An additional benefit to comparing to the FIRST  $dN/dS$  is that the radio source counts at 1.4 GHz have been well quantified and modeled by numerous observations from Jy level down to sub-mJy depths (e.g., Windhorst et al. 1985; White et al. 1997;

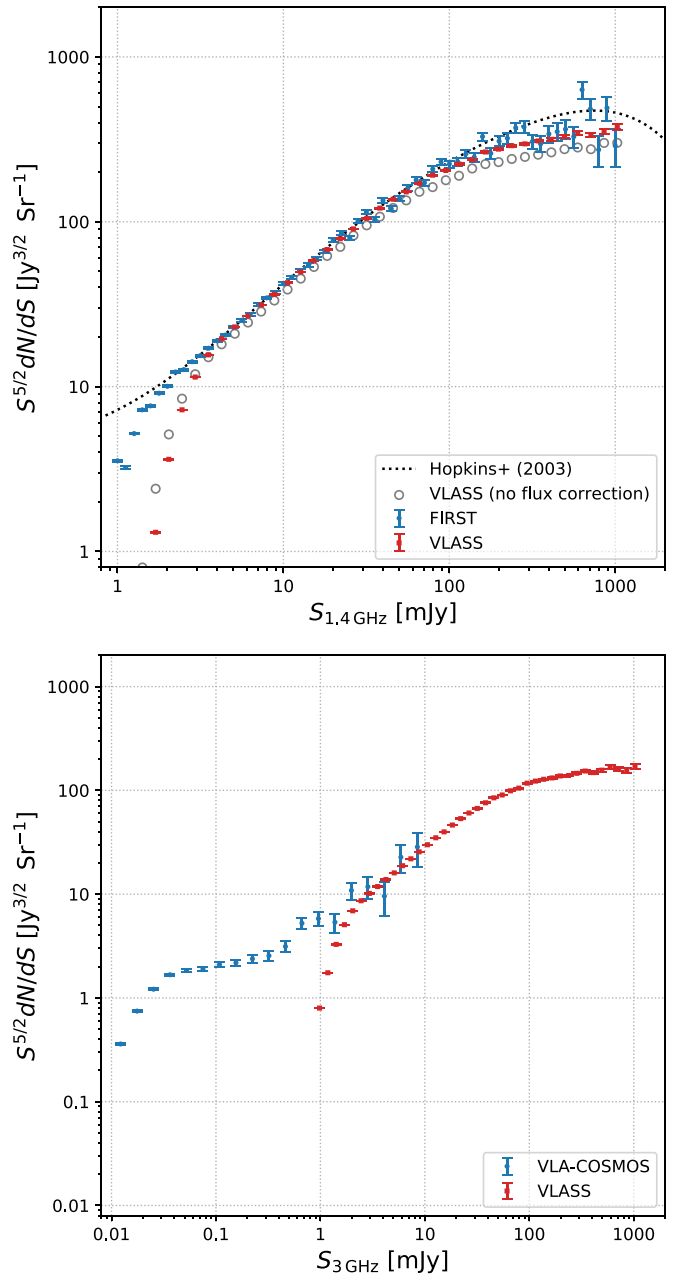


**Figure 13.** The Euclidean normalized differential source counts,  $dN/dS$ , for VLASS. The top panel shows VLASS converted to 1.4 GHz for comparison with FIRST (blue circles). The red squares show the VLASS source counts after scaling the cataloged flux density by 15% as derived in Section 3.2.2. The gray open circles show the VLASS  $dN/dS$  without correcting for the VLASS flux underestimate. For reference the black dotted line shows the sixth-order polynomial fit derived by Hopkins et al. (2003). In the bottom panel we show the VLASS  $dN/dS$  at 3 GHz (red squares) alongside the VLA-COSMOS source counts (blue circles).

Hopkins et al. 2003). Here we find that at  $S_{1.4 \text{ GHz}} \gtrsim 5 \text{ mJy}$  the VLASS *Quick Look*  $dN/dS$  is consistent with both the FIRST differential source counts and the sixth-order polynomial fit to the 1.4 GHz  $dN/dS$  obtained by Hopkins et al. (2003). Assuming  $\alpha = -0.71$ , 5 mJy at 1.4 GHz is equivalent to 2.9 mJy at 3 GHz. The agreement with the 1.4 GHz source counts is also indicative that the VLASS flux calibration derived in Section 3.2.2 is accurate, and we show the 1.4 GHz  $dN/dS$  for VLASS using uncorrected flux measurements on this same plot for reference. The comparison with the  $dN/dS$  at

both 3 and 1.4 GHz as established by previous works is consistent with the VLASS *Quick Look* catalog being incomplete at flux densities below  $S_{3\text{ GHz}} \sim 3$  mJy.

## 6. The Sizes of Radio Sources

### 6.1. Angular Size Distribution of VLASS Components

With a median uncertainty of  $\sim 0.^{\circ}1$ , the distribution of deconvolved component sizes,  $\Psi$ , in VLASS probes down to a scale of  $\sim 0.^{\circ}3$ – $0.^{\circ}4$ . Below this, components are listed as having a zero size as observed in VLASS, and higher-resolution observations are required to measure their sizes. The distribution of the FWHM of the deconvolved major axis,  $\Psi_{\text{maj}}$ , of VLASS components with  $S_{\text{peak}} > 3$  mJy beam $^{-1}$  is shown in Figure 14. Here we denote the population of components where  $\Psi_{\text{maj}}$  is listed as zero in the bin at  $\Psi_{\text{maj}} = 0.^{\circ}03$ .

For those components with a measured, rather than zero, deconvolved angular size we can exploit the availability of this large high-resolution data set to investigate the relation between radio source size and total flux density (Windhorst et al. 1990) at  $\nu \sim 3$  GHz. In the bottom panel of Figure 14 we show the distribution of nonzero deconvolved VLASS component sizes as a function of total component flux. Our sample shows substantial scatter, but with a trend for increasing size with flux density. For  $S_{\text{total}} \lesssim 50$  mJy the median component size follows a trend of  $\Psi(S) \propto S^{0.3 \pm 0.01}$ , consistent with  $\Psi = 2''S_{1.4\text{ GHz}}^{0.3}$  reported by Windhorst et al. (1990). For VLASS components brighter than  $S \gtrsim 50$  mJy the slope of this trend flattens somewhat to  $\sim 0.2$ . However, this may be attributable to the VLASS survey design. VLASS is run in the VLA's B and BnA configurations.<sup>10</sup> One of the impacts of this observing mode is that sensitivity to large angular scale structure is reduced by a lack of short baselines used in the array configuration. In the case of VLASS this results in larger ( $\Psi \gtrsim 30''$ ) objects being resolved into multiple components or lost altogether (Lacy et al. 2020). As a consequence, VLASS will only sample components with small angular sizes at higher flux densities. A further effect is that the relationship between linear size and flux density is dependent on a source not being split into multiple components. Consequently, components detected in a high angular resolution such as VLASS are only suitable for testing this relation at small angular scales, and testing at large angular scales necessitates a sample of verified multicomponent sources.

### 6.2. The VLASS Two-point Correlation Function

The high resolution of VLASS lends itself to exploring small-scale clustering of radio detections. To this end we determine the angular two-point correlation function for VLASS using the Landy & Szalay (1993) estimator:

$$\xi_{\text{LS}} = \frac{DD - 2DR + RR}{RR}, \quad (3)$$

where  $DD$  is the real data autocorrelation,  $RR$  is the autocorrelation of random data, and  $DR$  is the cross-correlation of real and random data. Given that the angular resolution of VLASS is about twice that of FIRST, one might expect the two-point correlation functions of these surveys to diverge at angular scales below the FIRST beam size. To that end we

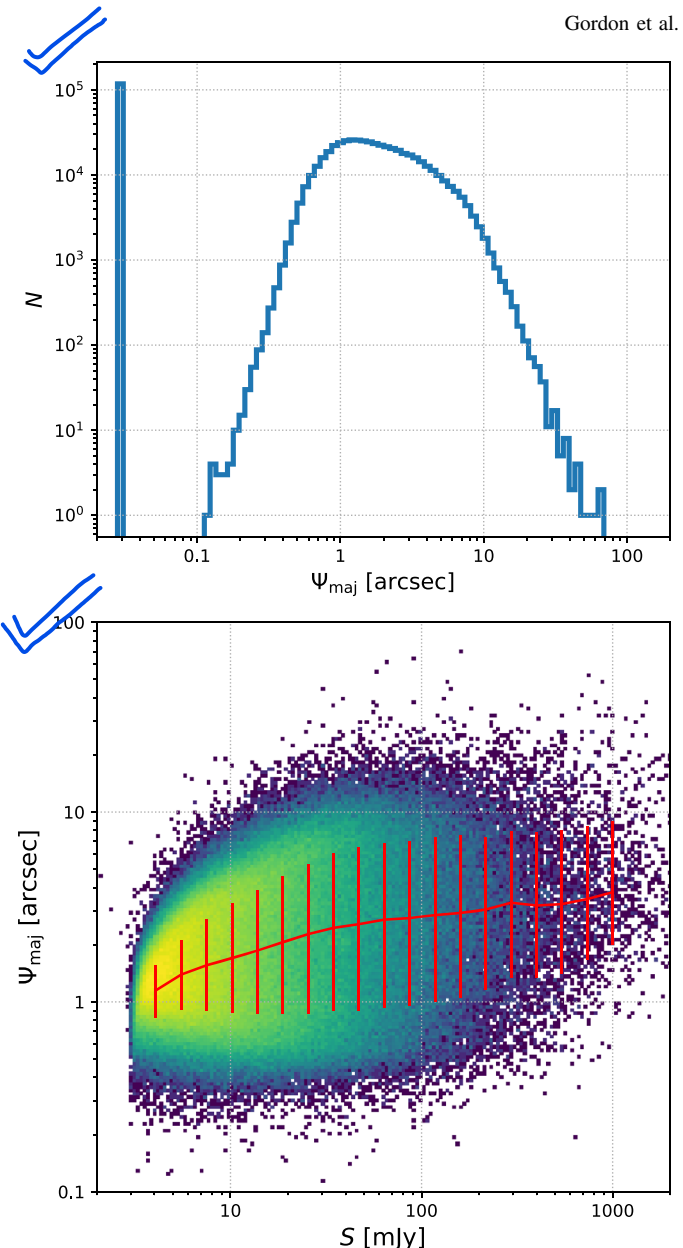


**Figure 14.** The angular size distributions of VLASS components with  $S_{\text{peak}} > 3$  mJy beam $^{-1}$ . The top panel shows a histogram of the deconvolved major axis size,  $\Psi_{\text{maj}}$ . The number of components with a size listed as zero in the catalog (i.e., smaller than can be measured by VLASS) is shown in the bin at  $0.^{\circ}03$ . The bottom panel shows the distribution of the deconvolved major axis for VLASS components with a nonzero cataloged size vs. component total flux density. The red line shows the median deconvolved angular size of the component for a particular flux bin. Error bars are defined by the 16th and 84th percentiles of the size distribution in each flux bin and broadly show a weak ( $r = 0.3$ ) correlation with flux with  $\Psi \propto S^{0.3}$  below 50 mJy.

additionally determine the FIRST two-point correlation function for comparison.

In Figure 15 we show both the VLASS and FIRST two-point correlation functions over the range  $0.^{\circ}0003$  ( $1.^{\circ}1$ )  $< \theta < 10^{\circ}$ . To compensate for incompleteness at low flux densities, only VLASS components with  $S_{3\text{ GHz}} > 3$  mJy are used in this analysis. To ensure a fair comparison with FIRST, we limit our two-point correlation for FIRST to components with  $S_{1.4\text{ GHz}} > 5$  mJy. We fit the VLASS two-point correlation with two power laws, such that

$$\xi(\theta) = A\theta^{\alpha} + B\theta^{\beta}, \quad (4)$$

<sup>10</sup> See [https://science.nrao.edu/facilities/vla/docs/manuals/propvla/array\\_configs](https://science.nrao.edu/facilities/vla/docs/manuals/propvla/array_configs) for more details on VLA observing configurations.

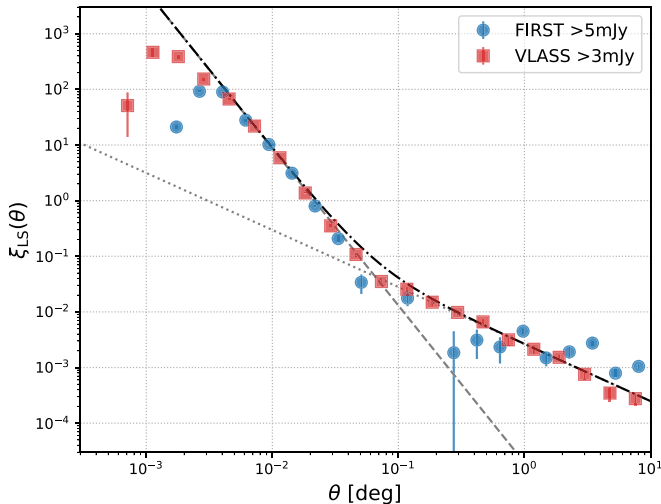


**Figure 15.** Two-point correlation for VLASS components with  $S_{\text{Total}} > 3 \text{ mJy}$  (red squares). For comparison the two-point correlation function for FIRST is also shown (blue circles). The VLASS two-point correlation shows excess power at  $\theta \lesssim 0.002$  ( $\sim 7''$ ) relative to FIRST, as expected given the higher resolution of VLASS. The black dashed line shows the sum of the two power laws fit to the VLASS two-point correlation function (see Table 4), while the gray dotted-dashed and dotted lines show the individual power laws fitted.

where  $A\theta^\alpha$  and  $B\theta^\beta$  are power-law fits at angular scales larger and smaller than  $0.05^\circ$ , respectively. For the VLASS *Quick Look* data,  $A = 2.6 \pm 0.3 \times 10^{-3}$ ,  $B = 1.9 \pm 0.3 \times 10^{-5}$ ,  $\alpha = -1.03 \pm 0.03$ , and  $\beta = -2.83 \pm 0.10$ . These parameters, as well as our determined values for the FIRST two-point correlation, are shown in Table 4, alongside the  $\chi^2$  values for the two power-law fits.

The VLASS two-point correlation function shows a slope of  $-1.03$  at angular scales greater than  $0.05^\circ$ . As expected, the gradient of the VLASS two-point correlation function steepens at  $\theta \lesssim 0.05$  to  $-2.83$ . This break is the result of radio sources being split into multiple components at smaller angular scales resulting in excess observed clustering (Cress et al. 1996; Blake & Wall 2002). Notably, the VLASS two-point correlation function shows excess power relative to FIRST at angular scales smaller than  $\theta \sim 0.002$  ( $\sim 7''$ ), the result of VLASS having twice the angular resolution of FIRST—multicomponent sources at this scale split by VLASS are usually observed as a single component by FIRST (see also Section 6.3). The excess power at small angular scales in the VLASS two-point correlation function demonstrates the potential to probe the angular size distribution of double radio sources down to the order of a few arcseconds with VLASS.

### 6.3. Splitting Close Doubles with VLASS

Given that VLASS has a similar sensitivity to FIRST but with twice as good an angular resolution, it stands to reason that some fraction of double radio galaxies that are observed as a single component in FIRST will be split into double or triple sources by VLASS. To test this, we take the AGN from the Best & Heckman (2012) catalog of radio galaxies that are associated with a single FIRST component. Using these data has the double advantage that (a) the radio observations have been associated with a host galaxy already and (b) the radio emission has been identified as being due to an AGN, rather than star formation, and thus is potentially an unresolved

**Table 4**  
Power-law Parameters for Equation (4) Determined from Both VLASS and FIRST, and the  $\chi^2$  Value for the Fit to the Respective Data Set

	VLASS	FIRST
$A (\times 10^{-3})$	$2.6 \pm 0.3$	$2.0 \pm 0.3$
$\alpha$	$-1.03 \pm 0.03$	$-0.87 \pm 0.18$
$B (\times 10^{-5})$	$1.9 \pm 0.3$	$2.3 \pm 0.4$
$\beta$	$-2.83 \pm 0.10$	$-2.77 \pm 0.11$
$\chi^2$	2.82	1.59

double or triple radio source. To test this, we search a radius of  $10''$  around each of the 11,556 single-FIRST-component AGN in the Best & Heckman (2012) catalog, counting the number of matches within our catalog for each Best & Heckman (2012) source—those with multiple VLASS matches are likely to be sources that have been split into multiple components by VLASS. In Figure 16 we show six examples of single-FIRST-component AGN that are split into multiple components by VLASS (five doubles and one triple).

We find that 1011 single-FIRST-component AGN from Best & Heckman (2012) are split into multiple components by VLASS. Of these, 890 objects are split into two components, 110 sources are split into three components, 9 sources are split into four components, and 2 sources are split into five VLASS components. In Figure 17 we show the fraction of Best & Heckman (2012) single-FIRST-component AGN split into multiple components by VLASS as a function of the total flux density of that source in the FIRST catalog. At lower flux densities ( $1 \text{ mJy} \lesssim S_{1.4 \text{ GHz}} \lesssim 10 \text{ mJy}$ ) the fraction of resolved sources increases from 8% to  $\sim 20\%$  with increasing flux density. This trend of increasing resolved fraction is probably due to sensitivity and frequency differences between the surveys. For instance, a typical spectrum radio source with  $\alpha = -0.7$  and a  $1.4 \text{ GHz}$  flux density of  $1 \text{ mJy}$  would be expected to have a  $3 \text{ GHz}$  flux density of  $0.59 \text{ mJy}$ . If that source is then split into multiple components, the flux density of each component is naturally lower than the sum of the total source flux density—e.g., a  $0.6 \text{ mJy}$  source could be resolved into two components of  $0.3 \text{ mJy}$  each. At  $10 \text{ mJy} \lesssim S_{1.4 \text{ GHz}} \lesssim 100 \text{ mJy}$ , around 20% of single-FIRST-component AGN are split into multiple components by VLASS. For sources brighter than this, the resolved fraction tends to increase with flux density again. This is likely biased by false-positive detections near bright components that were not removed by our quality flagging. For example, sidelobes around sources brighter than  $S_{1.4 \text{ GHz}} > 100 \text{ mJy}$  are themselves bright enough that they may not be flagged by the catalog quality flagging algorithm. Such cases will contribute to a fraction of single-FIRST-component AGN that may appear to have multiple components in the VLASS *Quick Look* images and artificially inflate the resolved fraction. Taking sources with  $10 \text{ mJy} < S_{1.4 \text{ GHz}} < 100 \text{ mJy}$ ,  $17.7\% \pm 0.6\%$  of single-FIRST-component AGN are split into multiple components by VLASS.

As the Best & Heckman (2012) catalog includes spectroscopic data about the host galaxies, we can report on the properties of those radio galaxies split into multiple components by VLASS. The spectroscopic properties of these sources are of interest, as the AGN in low- and high-excitation radio galaxies (HERGs and LERGs, respectively) are expected to be powered by different accretion modes (e.g., Hardcastle et al. 2006, 2007; Buttiglione et al. 2010; Evans et al. 2011).

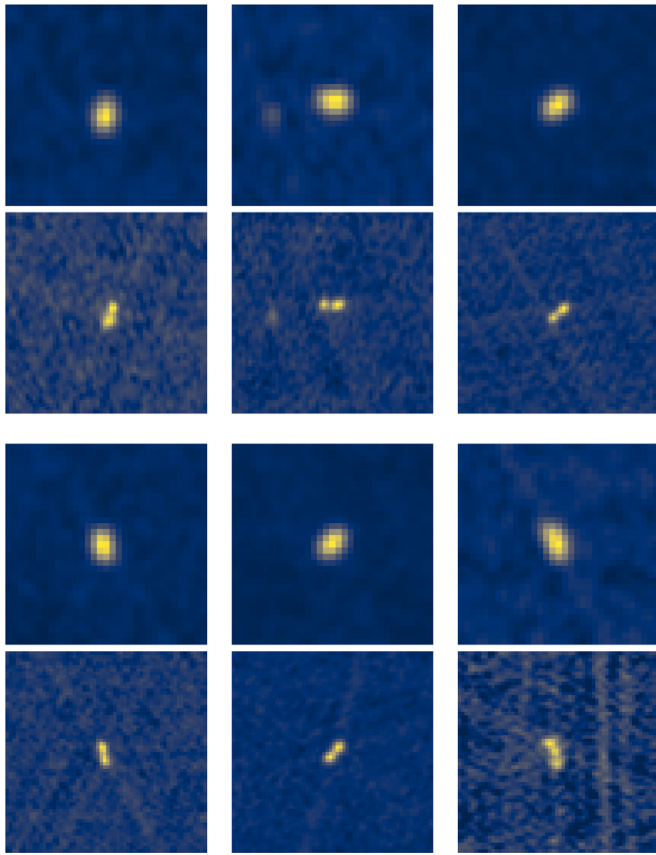


**Figure 16.** Six examples of single-FIRST-component AGN from Best & Heckman (2012) that are split into multiple components by VLASS. The postage stamp images are  $1' \times 1'$  and are arranged into two rows and three columns of paired images. The top panel in a pair shows the FIRST image, and the bottom panel shows the VLASS image. Five of the six examples show VLASS doubles, and the lower right image pair shows an example of a single-FIRST-component AGN split into a triple source by VLASS.

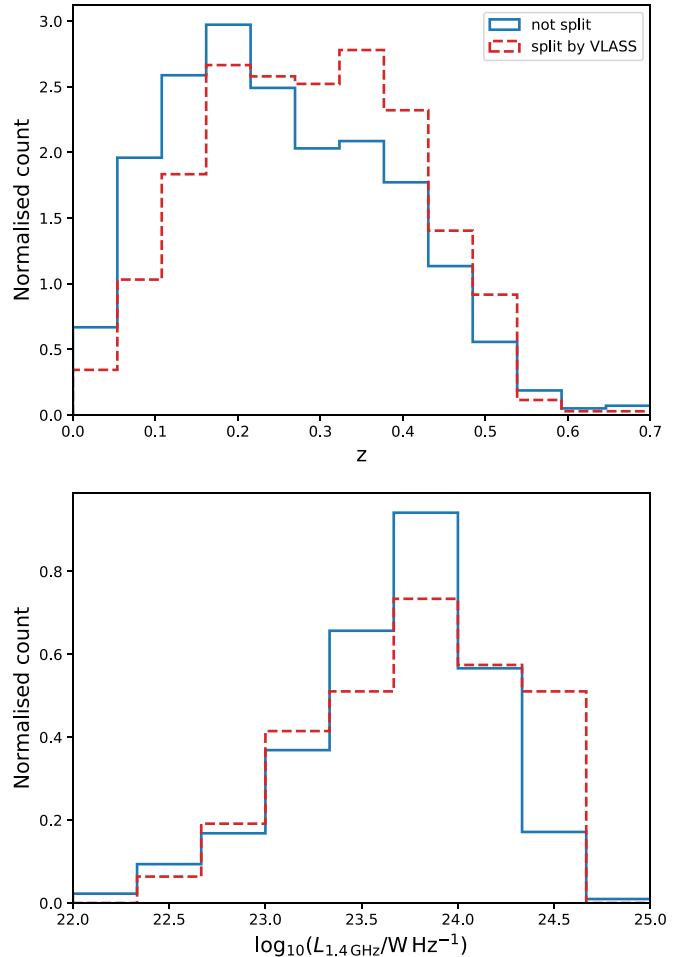


**Figure 18.** The top panel shows the normalized distributions of redshift for single-FIRST-component AGN from Best & Heckman (2012) with  $10 \text{ mJy} < S_{1.4 \text{ GHz}} < 100 \text{ mJy}$  (blue solid line) and the subset that is split into multiple components by VLASS (red dashed line). The bottom panel shows the distributions of  $1.4 \text{ GHz}$  luminosity for galaxies with  $z < 0.15$  within these samples.

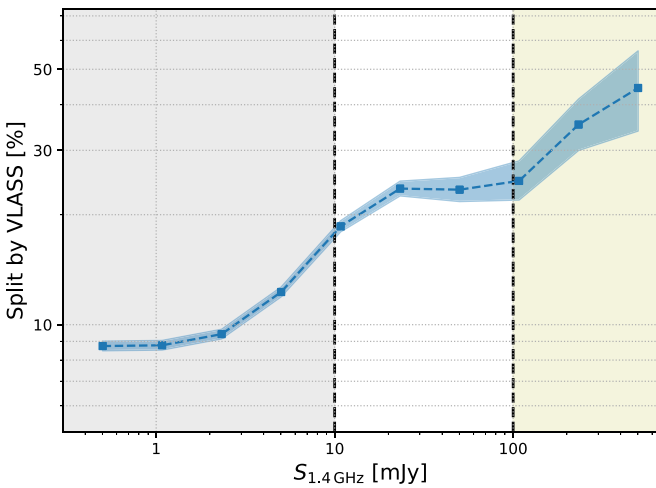


**Figure 17.** The percentage of AGN in the radio galaxy catalog of Best & Heckman (2012) associated with a single FIRST component that have been split into multiple components by VLASS plotted as a function of  $1.4 \text{ GHz}$  flux density. The gray shaded region to the left of both black dashed lines represents  $S_{1.4 \text{ GHz}} < 10 \text{ mJy}$ , where the combination of spectral index and spreading the emission across multiple components is expected to result in missed VLASS detections. The yellow shaded region to the right of both black dashed lines shows  $S_{1.4 \text{ GHz}} > 100 \text{ mJy}$ , where the high flux density of VLASS components may result in sidelobes contaminating the fraction of multi-VLASS-single-FIRST-component sources.

However, the splitting of single-FIRST-component AGN into multiple VLASS components is the combined result of the physical extent of the radio emission and the distance to the source. Spectroscopic incompleteness resulting from the latter of these factors could bias the spectroscopic classification in such a comparison. Indeed, considering only those sources with  $10 \text{ mJy} < S_{1.4 \text{ GHz}} < 100 \text{ mJy}$ , the redshift distribution of single-FIRST-component AGN split by VLASS differs from that of the general single-FIRST-component AGN (see Figure 18). Consequently, we focus on radio AGN at  $z < 0.15$  and  $10 \text{ mJy} < S_{1.4 \text{ GHz}} < 100 \text{ mJy}$  when comparing those single-FIRST-component sources split by VLASS ( $n = 94$ , hereafter referred to as the “split” sample) to the wider single-FIRST-component AGN population ( $n = 927$ , referred to as the “full” sample). Moreover, taking the minimum possible separation between split components to be the VLASS beam size of  $2.''5$  corresponds to a linear size of  $7.5 \text{ kpc}$  at a redshift of  $z = 0.15$ . Thus, VLASS can resolve radio lobes down to galactic scales, ostensibly FR0s (Baldi et al. 2018), in the local universe.

For the split sample,  $96.8^{+1.0}_{-2.9}\%$  are hosted by LERGs and  $1.1^{+2.4}_{-0.3}\%$  by HERGs (with the remainder unclassified). Comparably, LERGs and HERGs account for  $95.7^{+0.6}_{-0.8}\%$  and

$3.2^{+0.7}_{-0.5}\%$ , respectively, of the full sample. Additionally, the availability of redshift data for these objects allows us to report their radio luminosity. In Figure 18 we show the 1.4 GHz luminosity distributions of the split and full samples, calculated using the flux density of the FIRST component. The radio luminosity distributions of the two samples are statistically consistent, with a Kolmogorov–Smirnov test returning a *p*-value of 0.06. The similarity in both spectroscopic classifications and radio luminosity distributions of these two samples suggests that these two populations are hosted by physically alike AGN. This is consistent with previous studies showing that radio extent alone cannot distinguish between fundamentally different populations of AGN (e.g., Baldi et al. 2018; Capetti et al. 2020).

## 7. Summary

Using the VLASS epoch 1 *Quick Look* images, we have produced a catalog of radio components and characterized their quality. Using this, we have investigated the number counts and size distributions of radio components and sources at  $\nu \sim 3$  GHz. The key points of this work are as follows:

1. A catalog of  $1.9 \times 10^6$  reliable and unique detections from VLASS epoch 1 *Quick Look* imaging is available at <https://cirada.ca/catalogs>. Flux density measurements are underestimated by  $\sim 15\%$  above  $3 \text{ mJy beam}^{-1}$  and may be less reliable below this. For the statistical analyses presented in this work we compensate for this by scaling our flux densities accordingly, but this correction is not applied to the catalog data. Additionally, the astrometric accuracy of this catalog is limited to  $\sim 0.^{\circ}5$  at decl.  $> -20^{\circ}$  and  $\sim 1''$  at more southerly declinations.
2. Combining our catalog with FIRST shows that VLASS components at  $S_{3 \text{ GHz}} > 3 \text{ mJy beam}^{-1}$  have a typical spectral index of  $\alpha \sim -0.71$  between 1.4 and 3 GHz. Further combining with LoTSS DR1 demonstrates the potential for finding large numbers of radio sources with non-normal spectral curvature by utilizing upcoming survey data.
3. At  $S_{3 \text{ GHz}} \gtrsim 3 \text{ mJy}$  the VLASS  $dN/dS$  distribution is consistent with VLA-COSMOS, FIRST, and the sixth-order polynomial fit to 1.4 GHz observations from Hopkins et al. (2003). Our VLASS catalog is shown to suffer from incompleteness at  $S_{3 \text{ GHz}} < 3 \text{ mJy}$ .
4. The advantage of having higher angular resolution than FIRST is demonstrated via excess power in the VLASS two-point correlation function relative to FIRST at angular scales below  $\sim 10''$ . Moreover,  $\sim 20\%$  of AGN associated with a single FIRST component are split into multiple components using VLASS. At  $z < 0.15$ , single-FIRST-component AGN that are split into multiple components by VLASS have the same radio luminosities and spectral excitation state as those that are observed as a single component by VLASS.

Author note: After the public release of our VLASS *Quick Look* catalog, Gordon et al. (2020), and the completion of this manuscript based on those data, the authors have become aware of a second, independent VLASS catalog that has recently been made available to the community by Bruzewski et al. (2021).

The authors thank the anonymous referee for their constructive comments that have improved the quality of this work. We thank Mark Lacy for discussions about the quick look images, and additionally J. J. Kavelaars and Gilles Ferrand for their helpful feedback on the manuscript. Y.A.G., M.M.B., C.P.O., A.N.V., and S.A.B. are supported by NSERC, the Natural Sciences and Engineering Research Council of Canada. Partial support for L.R. comes from US National Science Foundation grant AST17-14205 to the University of Minnesota. H.A. benefited from grant CIIC 90/2020 of Universidad de Guanajuato.

The Canadian Initiative for Radio Astronomy Data Analysis (CIRADA) is funded by a grant from the Canada Foundation for Innovation 2017 Innovation Fund (Project 35999) and by the Provinces of Ontario, British Columbia, Alberta, Manitoba, and Quebec, in collaboration with the National Research Council of Canada, the US National Radio Astronomy Observatory, and Australia’s Commonwealth Scientific and Industrial Research Organisation.

This research used the facilities of the Canadian Astronomy Data Centre operated by the National Research Council of Canada with the support of the Canadian Space Agency.

In this work we have made use of data obtained by the VLA, LOFAR, WISE, and the Sloan Digital Sky Survey (SDSS). The National Radio Astronomy Observatory is a facility of the National Science Foundation operated under cooperative agreement by Associated Universities, Inc. LOFAR data products were provided by the LOFAR Surveys Key Science project (LSKSP; <https://lofar-surveys.org/>) and were derived from observations with the International LOFAR Telescope (ILT). LOFAR (van Haarlem et al. 2013) is the Low Frequency Array designed and constructed by ASTRON. It has observing, data processing, and data storage facilities in several countries, which are owned by various parties (each with their own funding sources), and which are collectively operated by the ILT foundation under a joint scientific policy. The efforts of the LSKSP have benefited from funding from the European Research Council, NOVA, NWO, CNRS-INSU, the SURF Co-operative, the UK Science and Technology Funding Council, and the Jülich Supercomputing Centre. This publication makes use of data products from the Wide-field Infrared Survey Explorer, which is a joint project of the University of California, Los Angeles, and the Jet Propulsion Laboratory/California Institute of Technology, and NEOWISE (Mainzer et al. 2011), which is a project of the Jet Propulsion Laboratory/California Institute of Technology. WISE and NEOWISE are funded by the National Aeronautics and Space Administration. Funding for the SDSS and SDSS-II has been provided by the Alfred P. Sloan Foundation, the Participating Institutions, the National Science Foundation, the U.S. Department of Energy, the National Aeronautics and Space Administration, the Japanese Monbukagakusho, the Max Planck Society, and the Higher Education Funding Council for England. The SDSS website is <http://www.sdss.org/>. The SDSS is managed by the Astrophysical Research Consortium for the Participating Institutions. The Participating Institutions are the American Museum of Natural History, Astrophysical Institute Potsdam, University of Basel, University of Cambridge, Case Western Reserve University, University of Chicago, Drexel University, Fermilab, the Institute for Advanced Study, the Japan Participation Group, Johns Hopkins University, the Joint Institute for Nuclear Astrophysics, the

Kavli Institute for Particle Astrophysics and Cosmology, the Korean Scientist Group, the Chinese Academy of Sciences (LAMOST), Los Alamos National Laboratory, the Max-Planck-Institute for Astronomy (MPIA), the Max-Planck-Institute for Astrophysics (MPA), New Mexico State University, The Ohio State University, University of Pittsburgh, University of Portsmouth, Princeton University, the United States Naval Observatory, and the University of Washington.

Astropy (Astropy Collaboration et al. 2013, 2018), matplotlib (Hunter 2007), TOPCAT (Taylor 2005).

## ORCID iDs

Yjan A. Gordon <https://orcid.org/0000-0003-1432-253X>  
 Michelle M. Boyce <https://orcid.org/0000-0001-5470-3084>  
 Christopher P. O'Dea <https://orcid.org/0000-0001-6421-054X>  
 Lawrence Rudnick <https://orcid.org/0000-0001-5636-7213>  
 Heinz Andernach <https://orcid.org/0000-0003-4873-1681>  
 Adrian N. Vantyghem <https://orcid.org/0000-0003-4227-4838>  
 Samar Safi-Harb <https://orcid.org/0000-0001-6189-7665>  
 Isabel Sander <https://orcid.org/0000-0002-4400-4703>

## References

- Abazajian, K. N., Adelman-McCarthy, J. K., Agüeros, M. A., et al. 2009, *ApJS*, **182**, 543  
 Allen, L. R., Brown, R. H., & Palmer, H. P. 1962, *MNRAS*, **125**, 57  
 Astropy Collaboration, Price-Whelan, A. M., Sipőcz, B. M., et al. 2018, *AJ*, **156**, 123  
 Astropy Collaboration, Robitaille, T. P., Tollerud, E. J., et al. 2013, *A&A*, **558**, A33  
 Baldi, R. D., Capetti, A., & Massaro, F. 2018, *A&A*, **609**, A1  
 Becker, R. H., White, R. L., & Helfand, D. J. 1995, *ApJ*, **450**, 559  
 Best, P. N., & Heckman, T. M. 2012, *MNRAS*, **421**, 1569  
 Best, P. N., Kauffmann, G., Heckman, T. M., & Ivezić, Ž. 2005, *MNRAS*, **362**, 9  
 Blake, C., & Wall, J. 2002, *MNRAS*, **337**, 993  
 Bock, D. C. J., Large, M. I., & Sadler, E. M. 1999, *AJ*, **117**, 1578  
 Bruzewski, S., Schinzel, F. K., Taylor, G. B., & Petrov, L. 2021, *ApJ*, **914**, 42  
 Buttiglione, S., Capetti, A., Celotti, A., et al. 2010, *A&A*, **509**, A6  
 Cameron, E. 2011, *PASA*, **28**, 128  
 Capetti, A., Brienza, M., Baldi, R. D., et al. 2020, *A&A*, **642**, A107  
 Carilli, C. L., Ivison, R. J., & Frail, D. A. 2003, *ApJ*, **590**, 192  
 Condon, J. J., Cotton, W. D., & Broderick, J. J. 2002, *AJ*, **124**, 675  
 Condon, J. J., Cotton, W. D., Greisen, E. W., et al. 1998, *AJ*, **115**, 1693  
 Cotton, W. D., Condon, J. J., Kellermann, K. I., et al. 2018, *ApJ*, **856**, 67  
 Cress, C. M., Helfand, D. J., Becker, R. H., Gregg, M. D., & White, R. L. 1996, *ApJ*, **473**, 7  
 Cutri, R. M., Wright, E. L., Conrow, T., et al. 2013, yCat, II/328  
 de Gasperin, F., Intema, H. T., & Frail, D. A. 2018, *MNRAS*, **474**, 5008  
 Evans, D. A., Summers, A. C., Hardcastle, M. J., et al. 2011, *ApJL*, **741**, L4  
 Gaia Collaboration, Brown, A. G. A., Vallenari, A., et al. 2018, *A&A*, **616**, A1  
 Gaia Collaboration, Prusti, T., de Bruijne, J. H. J., et al. 2016, *A&A*, **595**, A1  
 Gordon, Y. A., Boyce, M. M., O'Dea, C. P., et al. 2020, *RNAAS*, **4**, 175  
 Hardcastle, M. J., Evans, D. A., & Croston, J. H. 2006, *MNRAS*, **370**, 1893  
 Hardcastle, M. J., Evans, D. A., & Croston, J. H. 2007, *MNRAS*, **376**, 1849  
 Harwood, J. J., Hardcastle, M. J., Morganti, R., et al. 2017, *MNRAS*, **469**, 639  
 Hopkins, A. M., Afonso, J., Chan, B., et al. 2003, *AJ*, **125**, 465  
 Hunter, J. D. 2007, *CSE*, **9**, 90  
 Intema, H. T., Jagannathan, P., Mooley, K. P., & Frail, D. A. 2017, *A&A*, **598**, A78  
 Jarrett, T. H., Cohen, M., Masci, F., et al. 2011, *ApJ*, **735**, 112  
 Jarrett, T. H., Cluver, M. E., Magoulas, C., et al. 2017, *ApJ*, **836**, 182  
 Johnston, S., Bailes, M., Bartel, N., et al. 2007, *PASA*, **24**, 174  
 Jonas, J. L. 2009, *IEEEP*, **97**, 1522  
 Kauffmann, G., Heckman, T. M., White, S. D. M., et al. 2003, *MNRAS*, **341**, 33  
 Kharb, P., O'Dea, C. P., Baum, S. A., et al. 2008, *ApJS*, **174**, 74  
 Kimball, A. 2017, VLASS Project Memo #7: VLASS Tiling and Sky Coverage, [https://library.nrao.edu/public/memos/vla/vlass/VLASS\\_007.pdf](https://library.nrao.edu/public/memos/vla/vlass/VLASS_007.pdf)  
 Lacy, M., Baum, S. A., Chandler, C. J., et al. 2020, *PASP*, **132**, 035001  
 Lacy, M., Meyers, S. T., Chandler, C., et al. 2019, VLASS Project Memo #13: Pilot and Epoch 1 Quick Look Data Release, [https://library.nrao.edu/public/memos/vla/vlass/VLASS\\_013.pdf](https://library.nrao.edu/public/memos/vla/vlass/VLASS_013.pdf)  
 Landy, S. D., & Szalay, A. S. 1993, *ApJ*, **412**, 64  
 Mainzer, A., Bauer, J., Grav, T., et al. 2011, *ApJ*, **731**, 53  
 Mauch, T., Murphy, T., Buttery, H. J., et al. 2003, *MNRAS*, **342**, 1117  
 McConnell, D., Hale, C. L., Lenc, E., et al. 2020, *PASA*, **37**, e048  
 Mohan, N., & Rafferty, D. 2015, PyBDSF: Python Blob Detection and Source Finder, Astrophysics Source Code Library, ascl:1502.007  
 Mooley, K. P., Hallinan, G., Bourke, S., et al. 2016, *ApJ*, **818**, 105  
 Norris, R. P. 2017, *NatAs*, **1**, 671  
 Norris, R. P., Hopkins, A. M., Afonso, J., et al. 2011, *PASA*, **28**, 215  
 Nyland, K., Dong, D. Z., Patil, P., et al. 2020, *ApJ*, **905**, 74  
 O'Dea, C. P. 1998, *PASP*, **110**, 493  
 O'Dea, C. P., & Saikia, D. J. 2021, *A&ARv*, **29**, 3  
 Oosterbaan, C. E. 1978, *A&A*, **69**, 235  
 Owen, F. N., & Morrison, G. E. 2008, *AJ*, **136**, 1889  
 Padovani, P. 2016, *A&ARv*, **24**, 13  
 Prandoni, I., Parma, P., Wieringa, M. H., et al. 2006, *A&A*, **457**, 517  
 Rengelink, R. B., Tang, Y., de Bruyn, A. G., et al. 1997, *A&AS*, **124**, 259  
 Sabater, J., Best, P. N., Tasse, C., et al. 2021, *A&A*, **648**, A2  
 Shimwell, T. W., Röttgering, H. J. A., Best, P. N., et al. 2017, *A&A*, **598**, A104  
 Shimwell, T. W., Tasse, C., Hardcastle, M. J., et al. 2019, *A&A*, **622**, A1  
 Smirnov, O. M. 2011a, *A&A*, **527**, A107  
 Smirnov, O. M. 2011b, *A&A*, **531**, A159  
 Smolčić, V., Novak, M., Bondi, M., et al. 2017, *A&A*, **602**, A1  
 Taylor, M. B. 2005, in ASP Conf. Ser., 347, Astronomical Data Analysis Software and Systems XIV, ed. P. Shopbell, M. Britton, & R. Ebert (San Francisco, CA: ASP), 29  
 van Haarlem, M. P., Wise, M. W., Gunst, A. W., et al. 2013, *A&A*, **556**, A2  
 Vernstrom, T., Scott, D., Wall, J. V., et al. 2016, *MNRAS*, **461**, 2879  
 White, R. L., Becker, R. H., Helfand, D. J., & Gregg, M. D. 1997, *ApJ*, **475**, 479  
 Whittam, I. H., Jarvis, M. J., Green, D. A., Heywood, I., & Riley, J. M. 2017, *MNRAS*, **471**, 908  
 Whittam, I. H., Riley, J. M., Green, D. A., et al. 2013, *MNRAS*, **429**, 2080  
 Windhorst, R., Mathis, D., & Neuschaefer, L. 1990, in ASP Conf. Ser., 10, Evolution of the Universe of Galaxies, ed. R. G. Kron (San Francisco, CA: ASP), 389  
 Windhorst, R. A., Miley, G. K., Owen, F. N., Kron, R. G., & Koo, D. C. 1985, *ApJ*, **289**, 494  
 Wright, E. L., Eisenhardt, P. R. M., Mainzer, A. K., et al. 2010, *AJ*, **140**, 1868  
 York, D. G., Adelman, J., Anderson, J. E. J., et al. 2000, *AJ*, **120**, 1579